One Earth

Article

Brown carbon from biomass burning imposes strong circum-Arctic warming

Graphical abstract

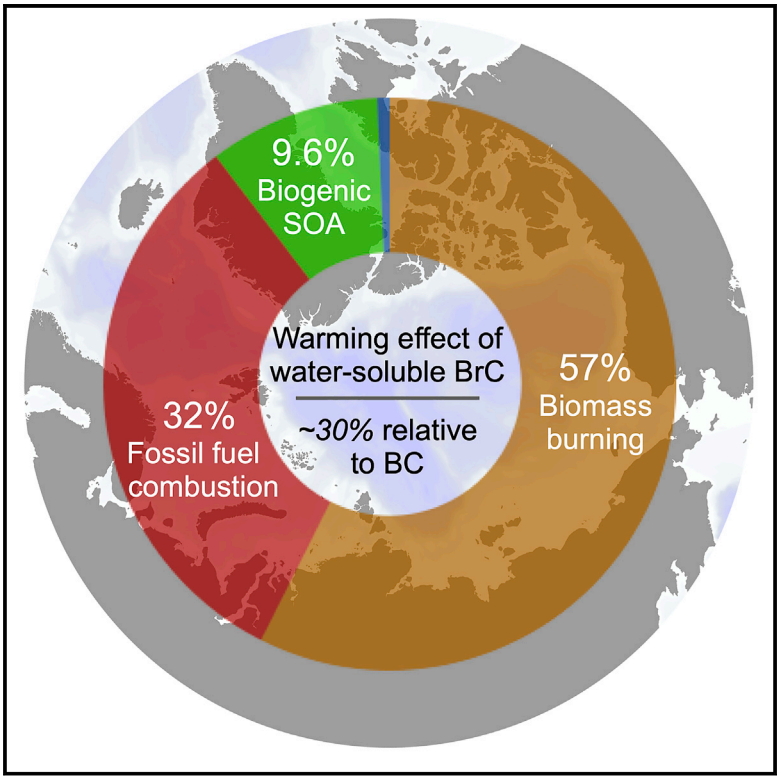

Authors

Siyao Yue, Jialei Zhu, Shuang Chen, ..., Meinrat O. Andreae, Yafang Cheng, Pingqing Fu

Correspondence

yafang.cheng@mpic.de (Y.C.), fupingqing@tju.edu.cn (P.F.)

In brief

The Arctic is warming at an excessive rate of more than three times as fast as the rest of the globe, exerting strong impacts on the Earth's climate, as well as on ecosystems and the economy. Identifying the warming agents is key to understanding Arctic warming and identifying mitigation solutions. We show that brown carbon, mainly from biomass burning, can impose strong circum-Arctic warming.

Highlights

- Brown carbon imposes strong Arctic warming
- Warming effect of water-soluble brown carbon is ~30% relative to black carbon
- Biomass burning contributes ~60% of the warming effect of brown carbon
- Warming climate leads to increased wildfires that reinforce Arctic warming

Yue et al., 2022, One Earth *5*, 293–304
March 18, 2022
https://doi.org/10.1016/j.oneear.2022.02.006

CellPress

One Earth

CellPress
OPEN ACCESS

Article

Brown carbon from biomass burning imposes strong circum-Arctic warming

Siyao Yue,[1,2,3,10] Jialei Zhu,[1,10] Shuang Chen,[1] Qiaorong Xie,[1] Wei Li,[4] Linjie Li,[3,11] Hong Ren,[1,3] Sihui Su,[1] Ping Li,[3] Hao Ma,[1] Yanbing Fan,[1] Borong Cheng,[1] Libin Wu,[1] Junjun Deng,[1] Wei Hu,[1] Lujie Ren,[1] Lianfang Wei,[3] Wanyu Zhao,[3] Yu Tian,[3] Xiaole Pan,[3] Yele Sun,[3] Zifa Wang,[3] Fengchang Wu,[5] Cong-Qiang Liu,[1] Hang Su,[6] Joyce E. Penner,[7] Ulrich Pöschl,[6] Meinrat O. Andreae,[6,8] Yafang Cheng,[2,9,*] and Pingqing Fu[1,3,12,*]

[1]Institute of Surface-Earth System Science, School of Earth System Science, Tianjin University, Tianjin 300072, China
[2]Minerva Research Group, Max Planck Institute for Chemistry, 55128 Mainz, Germany
[3]State Key Laboratory of Atmospheric Boundary Layer Physics and Atmospheric Chemistry, Institute of Atmospheric Physics, Chinese Academy of Sciences, Beijing 100029, China
[4]Third Institute of Oceanography, Ministry of Natural Resources, Xiamen 361005, China
[5]State Key Laboratory of Environmental Criteria and Risk Assessment, Chinese Research Academy of Environmental Sciences, Beijing 100012, China
[6]Multiphase Chemistry Department, Max Planck Institute for Chemistry, 55128 Mainz, Germany
[7]Department of Climate and Space Sciences and Engineering, University of Michigan, Ann Arbor, MI 48109, USA
[8]Department of Geology and Geophysics, King Saud University, Riyadh 11451, Saudi Arabia
[9]Department of Precision Machinery and Precision Instrumentation, University of Science and Technology of China, Hefei 230026, China
[10]These authors contributed equally
[11]Present address: Department of Chemistry and Molecular Biology, University of Gothenburg, 412 96 Gothenburg, Sweden
[12]Lead contact
*Correspondence: yafang.cheng@mpic.de (Y.C.), fupingqing@tju.edu.cn (P.F.)
https://doi.org/10.1016/j.oneear.2022.02.006

SCIENCE FOR SOCIETY Rapid Arctic warming and associated glacier and sea ice melt have a great impact on the global environment, with implications for global temperature rise and weather patterns, shipping routes, local biodiversity, and methane release. Greenhouse gases and black carbon aerosols are well-known warming agents that accumulate in the Arctic atmosphere, but full warming agent picture remains incomplete, preventing accurate forecasts. The effects of brown carbon—an aerosol derived from biomass and fossil fuel burning—are particularly unclear. Through observations from a circum-Arctic cruise and numerical model simulations, we show that light-absorbing brown carbon, mainly from biomass burning, can impose a strong warming effect in the Arctic, especially in the summertime. If, as predicted, the frequency, intensity, and spread of wildfires continues to increase, this may reinforce circum-Arctic warming and further contribute to global warming, forming a positive feedback. In light of these results, the careful management of vegetation fires, especially in the mid- to high latitudes of the Northern Hemisphere, will prove important in mitigating the warming in the Arctic region.

SUMMARY

Rapid warming in the Arctic has a huge impact on the global environment. Atmospheric brown carbon (BrC) is one of the least understood and uncertain warming agents due to a scarcity of observations. Here, we performed direct observations of atmospheric BrC and quantified its light-absorbing properties during a 2-month circum-Arctic cruise in summer of 2017. Through observation-constrained modeling, we show that BrC, mainly originated from biomass burning in the mid- to high latitudes of the Northern Hemisphere (~60%), can be a strong warming agent in the Arctic region, especially in the summer, with an average radiative forcing of ~90 mW m^{-2} (~30% relative to black carbon). As climate change is projected to increase the frequency, intensity, and spread of wildfires, we expect BrC to play an increasing role in Arctic warming in the future.

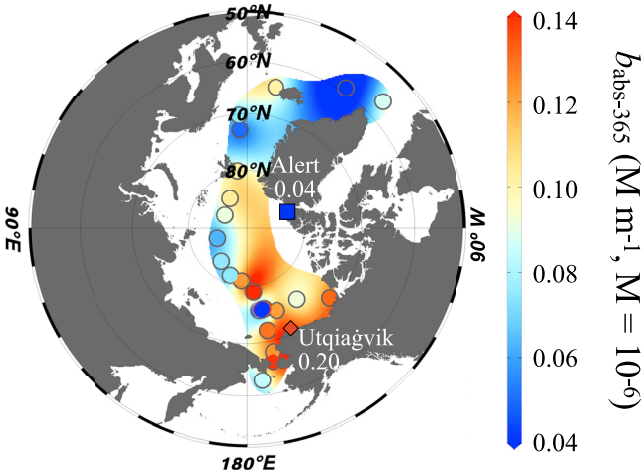

Figure 1. Geographical distribution of the measured mass light absorption coefficient (at 365 nm, $b_{abs-365}$, Mm^{-1}, M = 10^{-6}) of water-soluble BrC in the circum-Arctic

The data dots are plotted at the middle of each sample. The full cruise route for these samples is shown in Figure S1. The shading was interpolated based on the measurements using the Data-Interpolating Variational Analysis method in the software Ocean Data View.[38] The color range is set as the 10th and 90th percentiles of $b_{abs-365}$. The observed $b_{abs-365}$ of water-soluble BrC at Utqiaġvik (formerly Barrow) from August to September (2012) for PM_{10} samples (diamond)[35] and at Alert from May to early June (1991) for total suspended samples (square)[12] is also shown for comparison.

INTRODUCTION

The Arctic is warming at an excessive rate of more than twice as fast as the rest of the globe,[1,2] exerting strong impacts on the Earth climate[3–5] as well as on ecosystems[6] and economy.[7,8] Identifying the warming agents is key to understanding the Arctic warming and finding potential mitigation solutions. Among the various warming agents, brown carbon (BrC) remains one of the least understood and most uncertain contributors in the Arctic and surrounding regions. Its warming effect is either ignored in climate models[9,10] or estimated with large uncertainties, with contributions varying by a factor of 10 between studies, ranging from ~3% to >50% relative to the warming effect of black carbon (BC).[11–17]

Biomass burning and fossil fuel combustion are major sources of primary BrC and precursors of secondary BrC.[18–20] Natural and anthropogenic activities of these emissions have been intensifying in the Arctic and surrounding regions, e.g., from wildfires in Siberia and North America[21–23] and from shipping and industrialization,[24,25] respectively. These may increase the abundance of BrC in the Arctic.

The high uncertainty in the estimation of BrC radiative forcing stems from both insufficient observations and shortcomings in modeling. Currently, observations of BrC in the Arctic are spatially limited,[12,13,26–29] hindering representative assessment of its warming effect in the circum-Arctic. Furthermore, current models have often assumed that the absorption coefficient of BrC is independent of location[30,31] or parameterized the absorption of BrC as a function of the ratio of BC to organic aerosol in the source region,[32–34] rather than from direct measurements in the Arctic.

Here, we assess the warming impact of BrC by improving both observation and modeling. The light absorption of BrC was measured for the water extracts of aerosol samples (particulate diameter <10 μm [PM_{10}]; n = 25) collected from late July to September 2017 during a circum-Arctic cruise (north of 60°N; Figure S1; Table S1). Source-specific, light-absorbing properties of BrC (i.e., the imaginary part of refractive index [R_i]) are derived and used as constraints in the Community Earth System Model coupled with IMPACT aerosol model (CESM/IMPACT) to evaluate the overall and source-specific impact of BrC on circum-Arctic warming. Molecular-level measurements of particle composition by Fourier transform ion cyclotron resonance mass spectrometry (FT-ICR MS) are used to support the diagnosis of the major sources of the light absorption of BrC. Note that, in this study, we mainly focus on the warming effect of water-soluble BrC; however, water-insoluble BrC may also contribute significantly to light absorption and further increase the importance of BrC in the Arctic warming (see the discussion in the conclusions section).

RESULTS AND DISCUSSION

Light absorption of BrC

As shown in Figure 1, the light absorption coefficient of water-soluble BrC at 365 nm ($b_{abs-365}$) varies spatially from 0.02 to 0.26 Mm^{-1} in the circum-Arctic (Table S2). The average $b_{abs-365}$ of water-soluble BrC (0.10 ± 0.05 Mm^{-1}) over the Arctic region is higher than the 0.04 M m^{-1} observed at Alert (82.5°N) from May to early June[12] and lower than the 0.20 M m^{-1} observed at Utqiaġvik, Alaska (71.3°N) in August-September.[35] Since the Arctic is more vulnerable and sensitive to warming,[1,2] even though the absolute absorption coefficient of BrC in the Arctic is much lower than that in polluted areas, e.g., Xi'an in China (25 ± 12 M m^{-1})[36] and Patiala in India (40 ± 18 M m^{-1}),[37] the warming effect of BrC may have a strong impact in the Arctic and surrounding regions.

To constrain the light absorption parameters used in the model and reduce the uncertainty in the estimation of the radiative effect of BrC, we derived the light-absorbing properties of the water-soluble BrC from different sources based on our measurements in the Arctic. The large spatial variation in source-specific mass absorption efficiency at 365 nm (MAE_{365}) (Figure S3) reflects various contributing sources and mixtures of water-soluble BrC components in the Arctic. Here, water-soluble BrC is an operational term that refers to all the light-absorbing carbons in the water-soluble organic carbon (WSOC) (see experimental procedures). The sources of water-soluble BrC are resolved by apportioning WSOC via positive matrix factorization of typical tracers for fossil fuel combustion, biomass burning, secondary formation, primary biological particles, and marine aerosols (see experimental procedures).[39–41] The contribution profiles of the resolved sources vary between samples (Figure S5). The main sources of WSOC are identified as biogenic secondary organic aerosols (BSOAs) (average mass contribution ± one SD: 42% ± 23%), marine secondary aerosol (23% ± 18%), marine primary emission (14% ± 13%), and fossil fuel combustion (13% ± 14%), followed by biomass burning (6.8% ± 4.3%) and biological aerosol (i.e., bioaerosol; 2.6% ± 8.2%; Table S7). The high mass contribution from the secondary formation

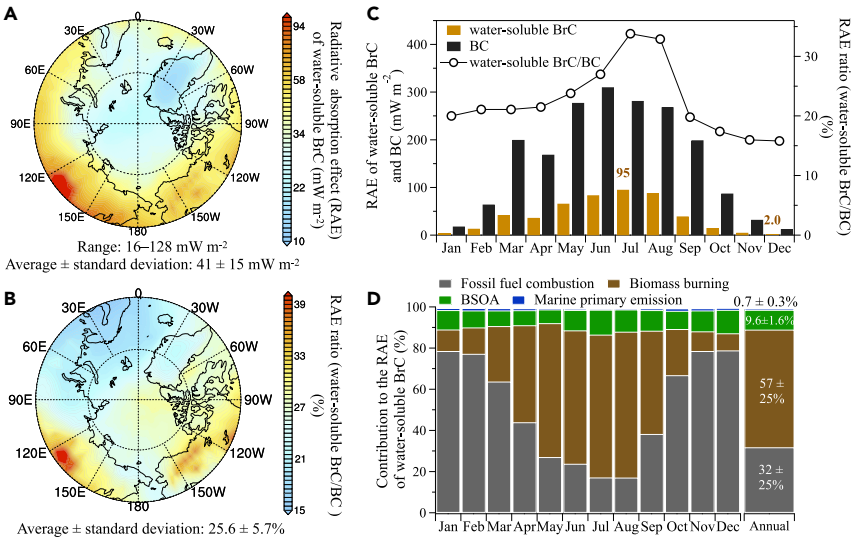

Figure 2. Strong impact of water-soluble BrC on simulated Arctic warming

(A) Annual average radiative absorption effect (RAE) of water-soluble BrC in the Arctic (north of 60°N).

(B) Annual average of the fractional RAE of water-soluble BrC relative to BC in the Arctic.

(C) Monthly variation of the RAE of water-soluble BrC and BC as well as the fractional RAE of water-soluble BrC relative to BC. The highest and lowest value for the monthly RAE of water-soluble BrC are shown for July and December, respectively.

(D) Monthly and annual average contribution from the four sources to the RAE of water-soluble BrC.

These plots present the strong impact of water-soluble BrC on circum-Arctic warming, especially the high contribution from biomass burning.

(BSOA and marine secondary aerosol) is expected in summer because of the enhanced photo-oxidation.[42]

The light-absorbing properties of water-soluble BrC from different sources are then derived by multivariate linear regression of b_{abs} on the source-specific WSOC concentrations (see experimental procedures). The linear regression can explain 83% of the variability of $b_{abs\text{-}365}$ (Figure S6). For our measurement locations and periods, the main contributors to $b_{abs\text{-}365}$ on average are fossil fuel combustion (41% ± 34%), BSOA (28% ± 24%), and biomass burning (27% ± 21%; Table S7). This source profile is ubiquitous from near UV to visible wavelengths (Figure S8). Marine primary emission and bioaerosol only account for 2.0% ± 2.8% and 1.6% ± 4.3%, respectively (Table S7).

Warming effect of BrC

To estimate the warming effect of BrC in the Arctic, we constrain the R_i of both water-soluble BrC and BC in the model based on our circum-Arctic measurements. The regression coefficients (i.e., MAE_{365}) for each source (Table S7) obtained from the multivariate linear regression are within the variations of those measured for source samples and field measurements at typical global hotspots of BrC[39] (Figure S7 and references therein). The wavelength-dependent imaginary R_is of the source-specific BrC are calculated from their MAEs and then used to constrain the model for assessing their climatic impact (experimental procedures). The wavelength dependencies of R_i for BrC from fossil fuel combustion, biomass burning, BSOA, and marine primary emission in the Arctic are determined by exponential fitting as shown in Figure S10. Note that we did not simulate bioaerosol in the model. While adding some uncertainty, its effect is not large, since the contribution from bioaerosol is very small, as shown above. The R*i* of BC is constrained to be 0.62 according to our measurement of optical properties of BC for the same samples during the circum-Arctic cruise (experimental procedures). We then used the CESM/IMPACT model with the measurement-based absorption properties of BrC and BC to examine the radiative effect of water-soluble BrC in the whole Arctic (north of 60°N) (experimental procedures). The model reliably reproduces the spatial distribution of OC concentrations compared with our measurements on the circum-Arctic cruise (Figure S11A). The average modeled OC concentration (0.60 ± 0.35 μgC m^{-3}) is only 5% smaller than that of the observed OC (0.63 ± 0.42 μgC m^{-3}; Table S2). Moreover, the modeled OC concentration shows a similar monthly variation as the observations at the Arctic Station Alert (Figure S11B).[12]

The radiative absorption effect (RAE) of water-soluble BrC is calculated as the difference in the incoming radiation flux at the top of atmosphere between model runs that include and exclude the light absorption of water-soluble BrC, respectively (experimental procedures). The annual average RAE of water-soluble BrC in the Arctic is 41 ± 15 mW m^{-2}, which varies from 16 to 128 mW m^{-2} (Figure 2A). Spatially, the strongest effect occurs in Siberia (up to ~100 mW m^{-2}) while the weakest is over Greenland (Figure 2A). The warming effect of water-soluble BrC is 26% ± 5.7% (Figure 2B) relative to that of BC (160 ± 49 mW m^{-2}; Figure S12). Compared with BC, the strongest relative effect of BrC occurs in Siberia (~40%), while the weakest is in western Europe (<20%; Figure 2B). The RAE of water-soluble BrC in the Arctic has a remarkable seasonal variation, with the strongest warming effect in summer (June to August) due to the increase in OC concentrations as well as in solar radiation. The average RAE in the Arctic in July is up to 95 mW m^{-2}, which is ~50 times that in December (2.0 mW m^{-2}) and dominates the annual warming (Figure 2C). In addition, the relative absorption effect from water-soluble BrC to that from BC increases to 31% in summer (Figure 2C). This is consistent with a case study at the Alert site from mid-May to early June (~34%).[12] Compared with lower latitudes, this relative RAE of water-soluble BrC to BC in the Arctic, even around the North Pole (~30%), is much higher than that in the East Asian outflow (2%–10%; spring),[43] the Himalayas (~4% ± 1%),[44] Xi'an (2% ± 1%; summer),[36] and New Delhi (3%–11%).[45] When the absorption effect of water-soluble BrC is included, the direct radiative effect of total OC in the Arctic changes from −231 ± 139 mW m^{-2} to −190 ± 144 mW m^{-2}, indicating an 18% warming effect by OC (Figure S13). These results demonstrate a strong impact of water-soluble BrC on circum-Arctic warming.

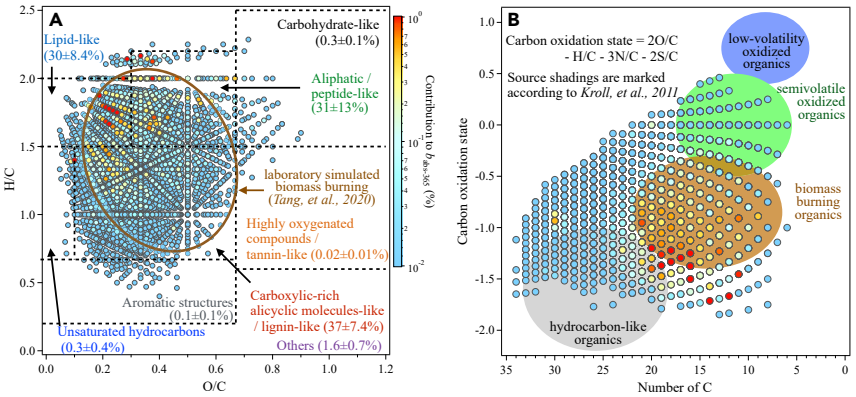

Figure 3. Molecular composition of the water-soluble organic aerosols and their contributions to light absorption ($b_{abs-365}$)

(A) Van Krevelen diagram of molecules (n = 4,148 molecules). The contributions to $b_{abs-365}$, averaged among samples, for each molecule are shown in color scale. The molecules are categorized into eight classes according to Bianco et al.[54] and Xie et al.[55] The fractional contributions to $b_{abs-365}$ are shown for each molecular class. The brown oval marks the region for water-soluble organics in simulated biomass burning aerosols according to Tang et al.[52]

(B) Carbon oxidation state-C-number space of molecules. The average molecular contributions among the samples to $b_{abs-365}$ are also shown in the same color scale as in (A). The source shadings are marked referring to Kroll et al.[53] Molecules with higher contributions are shown in the front in both plots. These plots show the strong contribution from biomass burning to the light absorption of water-soluble BrC.

Source identification

Different sources of water-soluble BrC contribute differently to its radiative absorption. During the observation period, the simulated RAE of water-soluble BrC at our sample locations is attributed to ~50% from fossil fuel combustion and ~40% from biomass burning, and the rest ~10% are from BSOA and marine primary emissions (Table S8), which is comparable to measurement results (Table S7). For the whole circum-Arctic, although in winter (December to February), fossil fuel combustion can be the dominant contributor (78%) to the RAE of water-soluble BrC, the total forcing is small compared with the warmer seasons. In summer, biomass burning contributes the most to the RAE of water-soluble BrC (up to ~70%), due to the high frequency of biomass burning in the mid- to high latitudes of the Northern Hemisphere (Figure S14; Table S10). On an annual average, water-soluble BrC from biomass burning contributes the largest fraction (~60%) to the total RAE in the circum-Arctic, while ~30% is attributed to fossil fuel combustion (Figure 2D). This highlights the strong impact of biomass burning on the Arctic warming, as summer is more relevant to ice-sheet melting. The lowest Arctic sea ice coverage usually occurs in summer and early fall and is therefore more sensitive to warming.[46] It is worth noting that, while the contribution of fossil fuel combustion is relatively small compared with biomass burning, light-absorbing particles from fossil fuel combustion, especially in winter, may also be important for summertime warming and sea ice and glacier melting because of their deposition on the snow and ice surface, which decreases the surface albedo and reduces the radiation reflected out of the Earth system.[47–49]

The high contribution of biomass burning to the RAE of water-soluble BrC is also reflected by the molecular-level light absorption apportionment based on FT-ICR MS measurements. The water-soluble content of aerosols was analyzed using FT-ICR MS with a wide detection mass range (150–1,000 Da). The light absorption of water-soluble BrC is apportioned to individual molecules by partial least-squares regression as in Zeng et al.[50] (see experimental procedures). Equivalent molecular absorption efficiencies of molecules are derived from this regression. The Van Krevelen diagram in Figure 3A shows the contribution of each molecule to $b_{abs-365}$. These molecules fall into eight categories. On average, carboxylic-rich alicyclic molecules-like/lignin-like (37% ± 7.4%), aliphatic/peptide-like (31% ± 13%), and lipid-like (30% ± 8.4%) compounds are the main contributors to the light absorption of water-soluble BrC (Figure 3A). In contrast, carbohydrate-like, unsaturated hydrocarbons, aromatic structures, highly oxygenated, tannin-like, and other compounds only contribute a small fraction (<3% in total). This contribution profile is consistent among samples (Figure S16). The three dominant molecular classes can be emitted in large amounts by biomass burning.[51,52] Figure 3B maps the molecules into an oxidation state-C number space, with regions indicating different aerosol sources, according to Kroll et al.[53] It also shows that the light absorption of water-soluble BrC is mainly contributed by organics from biomass burning. This molecular-level analysis by FT-ICR MS is consistent with the source contribution from the modeling, supporting the importance of biomass burning in the circum-Arctic warming.

CONCLUSIONS

Climate change in the Arctic is rapid and important to the entire world. This study highlights the large contribution of water-soluble BrC to Arctic warming using a model based on measurements of the optical parameters of water-soluble BrC in the circum-Arctic. We find that the radiative absorption effect of water-soluble BrC is strong in the Arctic, with an annual average of 26% ± 5.7% compared with BC and as high as 31% in summer. The model simulation indicates that the effect of water-soluble BrC on Arctic warming is dominated by BrC from biomass burning (~60%; annual average), especially in summer (up to ~70%), when the Arctic is more sensitive to warming (Figure 2D).

In this study, we mainly focused on water-soluble BrC; however, the light absorption of water-insoluble BrC may also play a role and contribute to the total radiative forcing. Further lab analyses show that, although the overall MAE_{365} of water-insoluble BrC (0.30 ± 0.26) is lower than that of the water-soluble BrC (0.56 ± 0.30), on average, the light absorption of water-insoluble BrC is ~80% of that of water-soluble BrC (Table S2). This means that, when the contribution of water-insoluble BrC is taken into account, the importance of the light absorption of BrC to the radiative forcing in the Arctic region will further increase by approximately 80% to about 74 mW m^{-2} (on average). As shown in Table S11, for total BrC, biomass burning is still the dominant source of the light absorption in the Arctic (~60%). But it should

be noted that further in-depth simulations are needed to have a more accurate estimation of the radiative effect of water-insoluble and total BrC.

Climate change is expected to increase the frequency, intensity, and spread of wildfires,[56–58] which in turn will reinforce the Arctic warming, forming a positive feedback.[59] We thus expect an increasing importance of BrC in the warming of the Arctic in future. Because biomass burning is also the major source of BC,[60] our results highlight the importance of managing vegetation fires, especially in the mid- to high latitudes of the Northern Hemisphere, in mitigating the warming in the Arctic region.

EXPERIMENTAL PROCEDURES

Resource availability

Lead contact

Further information and requests for resources and reagents should be directed to and will be fulfilled by the lead contact, Pingqing Fu (fupingqing@tju.edu.cn).

Materials availability

This study did not generate new unique materials.

Data and code availability

The data for the figures in the main text are available on the Zenodo repository: https://doi.org/10.5281/zenodo.6060440. All data are available from the corresponding author upon reasonable request or in the supplemental information. Custom code for this study is available from the corresponding author upon reasonable request.

Sampling

Ambient aerosol samples over the Arctic Ocean were collected on the research vessel *Xuelong* from 30 July to 24 September 2017 (Figure S1; Table S1). The cruise had a representative geographical coverage in the Arctic compared with previous studies at individual sites.[12,13,26–28] PM_{10} samples were collected onto prebaked (450°C for 6 h) quartz fiber filters (20 × 25 cm, TISSUQUARTZ-2500QAT-UP, Pallflex) by a high-volume sampler (Tisch 4,010,126, USA) at a flow rate 1.13 m^3 min^{-1}. Each sample was collected for around 2 days. Two field blanks were collected following the same procedure except for operating the pump. Samples and field blanks were stored in the dark at −20°C until analysis. The air mass sources were analyzed by backward trajectories utilizing the Hybrid Single-Particle Lagrangian Integrated Trajectory (HYSPLIT 4) model[61] (Figure S2).

WSOC and light absorption of water-soluble BrC

An aliquot of each sample and field blank was cut for the extraction of the water-soluble composition using 20 mL Milli-Q (18.2 MΩ/cm) water and ultrasonicated for 30 min. The extracts were then filtered via syringe-driven filters (Millex-GP, 0.22 μm, Millipore). One portion of the filtered extracts was measured for WSOC by a Total Organic Carbon analyzer (TOC-L, Shimadzu, Japan). Field blanks for WSOC accounted for 28% ± 13% of actual samples. The concentration of WSOC is reported after blank correction.

Light absorbance of water-soluble BrC was measured using another portion of the extracts by an ultraviolet-visible spectrophotometer (U3900H, Hitachi) in the range of 200–800 nm (step: 1 nm). Here, water-soluble BrC is an operational definition that includes all light-absorbing carbon in the water extracts. We retain using the terminology of WSOC when referring to mass concentrations and using water-soluble BrC when referring to the light-absorbing property. The absorption spectra were corrected against the blanks. The mass absorption coefficient ($b_{abs\text{-}\lambda}$, M m^{-1} = 10^{-6} m^{-1}) and mass absorption efficiency (MAE_λ, m^2 g^{-1}) are calculated to describe the optical properties of water-soluble BrC in the wavelength range of 280–500 nm.[43,62] These calculations are based on the measured light absorbance following previous methods (Equations 1 and 2).[12,62,63] The absorbance at 700 nm was subtracted to correct for the baseline drift during the measurement.

$$b_{abs-\lambda} = \frac{(A_\lambda - A_{700}) \times (V_{ext} \times f_{dil}) \times \ln 10}{V_{aero} \times L}, \quad \text{(Equation 1)}$$

where A_λ and A_{700} are the measured absorbances at wavelength λ nm (averaged between λ−5 nm and λ+5 nm) and 700 nm (averaged between 695 and 705 nm), respectively; V_{ext} is the volume of Milli-Q water used for the extraction; f_{dil} is the dilution factor; V_{aero} is the air volume; and L is the path length of the cuvette cell. MAE_λ is calculated using $b_{abs\text{-}\lambda}$ and the mass concentration of WSOC, expressed as follows:

$$MAE_\lambda = \frac{b_{abs-\lambda}}{WSOC}. \quad \text{(Equation 2)}$$

The wavelength dependence of the aerosol light absorption (b_{abs}) has often been described assuming a power-law relationship as follows:

$$b_{abs-\lambda} \propto \lambda^{-AAE}. \quad \text{(Equation 3)}$$

The parameter AAE is calculated by linear regression of log($b_{abs\text{-}\lambda}$) versus log(λ) between 300 and 400 nm. AAE_{BrC} can be used to extrapolate the optical properties of BrC to other wavelengths based on Equation 3. Values of b_{abs} and MAE below the measuring detection limits in the wavelength of 280–500 nm were estimated by using the value at an adjacent wavelength and this AAE.

Organic carbon and elemental carbon

OC and elemental carbon (EC) were measured by a thermal and optical carbon analyzer (OCEC Carbon Aerosol Analyzer, Model 5L, Sunset Laboratory, USA) using the NIOSH 870 method. A punch (1.5 cm^2) of each sample and field blank was used for the analysis. Based on filter blank uncertainties, the detection limits of OC and EC were approximately 93 ng C m^{-3} and 0.2 ng C m^{-3}, respectively. The equivalent OC and EC measurements of field blanks on average accounted for 19% ± 12% and 1.0% ± 3.5% of those of the actual samples, respectively. The concentrations of OC and EC were corrected against field blanks.

Organic molecular tracers

Procedures for the analysis of organic tracers have been documented in previous studies in detail.[64,65] Here, we measured molecular tracers for typical BrC sources in the samples. These tracers are sucrose, arabitol, trehalose, glucose, 2-methylglyceric acid (2-MGA), pinic acid, levoglucosan, mannosan, hopane C29αβ, and benzo[e]pyrene (BeP). Their corresponding sources are listed in Table S3. Briefly, an aliquot of each sample was cut into pieces and extracted three times with dichloromethane/methanol (2:1, v/v) under ultrasonication for 10 min. The solvent extracts were filtered through quartz wool, concentrated by a rotary evaporator, and blown down to dryness with nitrogen gas. Derivatization was then carried out by reaction with 50 μL of N,O-bis-(trimethylsilyl)trifluoroacetamide containing 1% trimethylsilyl chloride and 10 μL of pyridine at 70°C for 3 h. The derivatives were then mixed with 40 μL of n-hexane containing 1.43 ng μL^{-1} of the internal standard (C13 n-alkane). Gas chromatography/mass spectroscopy (GC/MS) analysis was performed using an Agilent GC (model 7890) coupled with Agilent Mass Selective Detector (model 5975C). The GC oven temperature was set to increase from 50°C (2 min) to 120°C at 15°C min^{-1} and then to 300°C at 5°C min^{-1} with a final isothermal hold at 300°C for 16 min. The carrier gas was helium (1.0 mL min^{-1}). The samples were injected with the injector temperature at 280°C. The mass spectrometer was operated on electron ionization mode at 70 eV and scanned between 50 and 650 Da. Data were processed using the Chemstation software. Individual compounds were identified by comparison of mass spectra with those of authenticated standards and literature data. Recoveries of the tracers were better than 80%. Field blanks were subtracted from real samples.

Ions. Methanesulfonic acid (MSA), chloride, sodium, and sulfate were measured by Ion Chromatography systems (Dionex Aquion, Thermo Scientific, USA) connected by one autosampler (Dionex AS-DV). Filter samples were ultrasonicated to extract the ions in Milli-Q water. Extracts were then filtered and analyzed by the ion chromatograph.

Source apportionment of WSOC

Positive matrix factorization (PMF)[66] was used to apportion the sources of WSOC, accordingly, the water-soluble BrC. The following species are selected

to be put into the PMF model: levoglucosan, mannosan, benzo[e]pyrene, hopane $C_{29}\alpha\beta$, 2-methylglyceric acid, pinic acid, glucose, trehalose, arabitol, sucrose, MSA, chloride, sodium, and sulfate. Their sources cover the main sources of WSOC and BrC according to Laskin et al.,[39] including biomass burning, fossil fuel combustion, biological emissions, marine primary emissions, and secondary formations.

To decompose the sources of WSOC, here, we combine the observations of WSOC with these source tracers. Their corresponding sources are listed in Table S3 based on the references therein. The reason to include biological aerosol tracers is that primary biological aerosols and secondary reactions of amino acids with ammonia have also been reported to be potential sources of BrC.[40,41,67] EPA PMF (v.5.0) allows using *a priori* information to constrain the modeling. The constraints of each chemical species in the factor profiles are shown in Table S4. Two hundred base runs were performed to find a global minimum. Then, constrained runs were performed until a converging run was found. The number of factors were determined combining the variation of Q/Q_{exp} (a ratio describing the explaining ability of adding factors on the variation of the input dataset) with the number of factors (Figure S4A) and the factor profile (Figure S4B).[66] $Q_{exp} \approx nm - p\,(n+m)$ denotes the degree of freedom of the model solution, where, n, m, and p are the number of samples, input tracers, and the number of factors. There is a smaller decrease in Q/Q_{exp} moving from eight to nine factors, suggesting eight factors are enough to explain the variability of the data.[66,68] The model captures well the variation of the input species as shown in the correlations between modeled and observed species (Table S5). The correlation between the measured and the modeled WSOC was 0.99 (R^2). A scatterplot for this correlation is shown in Figure S4C.

We use the bootstrapping (BS) and displacement (DISP) methods in EPA PMF to estimate the modeling uncertainty.[66,69] The diagnostics for error estimates are shown in Table S6 following the convention suggested by Brown et al.[66] There are no swaps for DISP and a lower decrease of Q by −0.05%. Overall, the error estimation by using the DISP and BS methods for our main target WSOC (Figure S4D) shows an acceptable output of the constrained base run.

The eight factors (i.e., sources) were diagnosed according to the main tracers in each factor (Figure S4B): (1) marine secondary aerosol, with MSA contributing around 75%; (2) marine primary emission, identified by chloride and sodium; (3) biomass burning, with levoglucosan and mannosan as indicators; (4) bioaerosol, with sucrose as the main contributor; (5) primary micro-organism and plankton indicated by arabitol, trehalose, and glucose; (6) BSOA indicated by pinic acid; and (7 and 8) two types of fossil fuel combustion (FF-1 and FF-2) indicated by hopane $C_{29}\alpha\beta$, BeP, and EC. The FF-1 contributed negligibly to WSOC, which suggests that it is the water-insoluble part of fossil fuel combustion. Except for primary micro-organism and plankton and FF-1, the other six sources contributed to WSOC by a non-negligible fraction (Figure S4B). In the following discussions, FF-2 will be termed fossil fuel combustion for simplicity. In summary, six sources are resolved for WSOC as fossil fuel combustion, biomass burning, BSOA, bioaerosol, marine primary emission, and marine secondary aerosol.

Source apportionment of water-soluble BrC

We then conduct multivariate least-squares linear regression with non-negative constraints on the coefficients between b_{abs} and the above source-apportioned WSOCs (Equation 4). MAEs of the water-soluble BrC from these sources are determined through the regression for individual wavelengths in the range of 280–500 nm. The Igor software (Wavemetrics) was used for this fitting. The regression coefficients were interpreted as the MAEs of each source. The light absorption of water-soluble BrC in the circum-Arctic are attributed to different sources using the WSOCs and their corresponding MAEs:

$$b_{abs} = \sum_i b_{abs,i} = \sum_i MAE_i \times WSOC_i. \quad \text{(Equation 4)}$$

This fitting was initially computed for the six sources of WSOC. As the fitting coefficient for marine secondary aerosol is <0.0001 $m^2\ g^{-1}$, it was subsequently omitted from the fitting due to its negligible contribution. The final fitting was conducted for the other five sources of WSOCs. The estimate of errors (SD) of these MAEs was produced by the fitting. The contributions of each source to the light absorption of water-soluble BrC were calculated using its MAE_i and mass concentration of $WSOC_i$. The imaginary part of the complex R_i of each source of water-soluble BrC was calculated according to Equation 5:[70]

$$Ri_\lambda = \frac{\rho_{particle} \times \lambda \times MAE_\lambda}{4\pi}, \quad \text{(Equation 5)}$$

where $\rho_{particle}$ is the density of the particle OC (assumed as 1.5 g cm^{-3}) and λ is the wavelength. Individual R_is for the five water-soluble BrC sources are calculated from the regressed MAEs at wavelengths from 280 to 500 nm. R_i is calculated from MAE at each wavelength. The SD of R_i is calculated from the estimated errors (SD) of MAEs based on error propagation. The relationship of R_i with wavelength is fitted with positive constraints for the fitting parameters. This fitting is weighted with the SD of R_i. The calculated R_is are used in the model simulation of the radiative effect of BrC.

Light absorption of BC

We measured the light absorption property of EC, a substitute for BC, by the Sunset Carbon analyzer according to the same method of previous studies.[12,71,72] The R_i of BC was derived and input as a constraint of the BC light absorption properties in the modeling. The attenuation coefficient of EC at 658 nm (i.e., $b_{atn\text{-}EC,\ 658}$) is calculated as follows:

$$b_{atn-EC,658} = \mathrm{ATN} \times \frac{A_{filter}}{V_{filter}}. \quad \text{(Equation 6)}$$

Here, *ATN* is the light attenuation measured by the analyzer. *A* and *V* correspond to the total area and volume of air filtered for each sample.

Then, the mass absorption coefficient ($b_{abs\text{-}EC,658}$, in M m^{-1}) is obtained by correcting $b_{atn\text{-}EC,658}$ for the "multiple scattering effect (*C*)" and the "shadowing effect, *R(ATN)*," according to the equation below:[72]

$$b_{abs-EC,658} = \frac{b_{atn-EC,658}}{C \times R(ATN)}. \quad \text{(Equation 7)}$$

These two effects represent two opposing processes on the measurement of light absorption. As the aerosol loading increases on a sample, the overall light absorption of EC increases. Simultaneously, due to the decrease in the effective path length, the light absorption of EC decreases.[72] A *C* value of 2.14 and 3.6 has been suggested for fresh and aged aerosols.[72] A value of $C = 3.6$ is used here for the Arctic aerosols, which are often transported from other regions[73] and exposed to relatively strong solar radiation in the warm season. The shadowing effect is calculated by an empirical relation using the measured *ATN* of EC, according to Weingartner et al.,[74]

$$R(ATN) = \left(\frac{1}{f} - 1\right) \times \left(\frac{\ln ATN - \ln 10}{\ln 50 - \ln 10}\right) + 1, \quad \text{(Equation 8)}$$

where *f* is set to 1.103 as reported by Ram and Sarin.[72] The mass absorption efficiency of EC at 658 nm ($MAE_{EC\text{-}658}$, $m^2\ g^{-1}$) is estimated based on the following equation:

$$MAE_{EC-658} = \frac{b_{abs-EC,658}}{EC}. \quad \text{(Equation 9)}$$

Then, R_i of EC at 658 nm is calculated using the same Equation 5 with a different density (1.8 g cm^{-3})[75,76] for EC. R_i is calculated to be 0.62 at 658 nm. Assuming an *AAE* of 1.0,[77] the R_i of EC is independent of wavelength according to Equations 2, 3, and 5.

Modeling of aerosol and radiative effect

The Community Earth System Model (CESM) v.1.2.2 coupled with the University of Michigan IMPACT aerosol model (CESM/IMPACT) with a resolution of 1.9 × 2.5°[31,78,79] is used to simulate the radiative effect of water-soluble BrC. In this model, sulfate in the nucleation (<5 nm), Aitken (5–50 nm), and accumulation (>50 nm) modes; soot from biomass burning (bSoot) (i.e., primary OC and BC from biomass burning); soot from fossil fuel and biofuel burning (fSoot) (i.e., primary OC and BC); and OC emitted from the ocean are simulated by one assumed size, while dust and sea salt are simulated in four separate size bins. Moreover, SOA formed from an explicit gas-phase chemical mechanism, including the oxidation of isoprene, α-pinene, and aromatics, and aqueous phase reactions of glyoxal and methylglyoxal are included. Organic nucleation is included to form new SOA particles, which are able to grow to Aitken and accumulation modes. The OC aerosol in this study includes primary OC from biomass and biofuel burning, fossil fuel combustion, and SOA as well as from the ocean. Details of the CESM/IMPACT model can be found in Zhu et al.[78–80]

We found that the percentage of water-soluble BrC in the OC is high before polar sunrise in March at the Arctic Station Alert and decreases with the enhancement of radiation and the melting of sea ice.[12,81] As a result, a fitted function of the daily maximum solar zenith angle fitting to the observations in the circum-Arctic (this study) and at Alert (82.5°N, 62.3°W; Figure S9)[12] as in the following is used to calculate the percentage of water-soluble BrC in the model.

$$f = -109.17cos(h) + 86.48, \quad \text{(Equation 10)}$$

where f is the percentage of water-soluble BrC in the OC and h is the daily maximum solar zenith angle.

An offline radiative transfer model is used to calculate aerosol optical properties and thus to estimate the aerosol direct radiative effects. The model was introduced in detail by Lin et al.[31] and Zhu et al.,[82] but the absorption property of water-soluble BrC from each source in the Arctic was updated based on the measurements in this study. The R_i of the internal mixtures within internally mixed aerosol were calculated by volume weighting of each of the individual aerosol species.

Two sets of schemes were designed to examine the radiative effect of water-soluble BrC. The ExBrC scheme assumed that all OC aerosol was not able to absorb radiation, i.e., water-soluble BrC was excluded, while the InBrC scheme includes water-soluble BrC with the percentage calculated following Equation 10. The measured R_is of water-soluble BrC from different sources were used to constrain the modeling. The parameters for water-soluble BrC from fossil fuel combustion, biomass burning, BSOA, and marine primary emission were included, but the parameter for water-soluble BrC from bioaerosol was not included because the model does not yet have the ability to simulate bioaerosol until now. However, this uncertainty is negligible because the contribution of bioaerosol is small, as discussed in the main text. The R_i of water-soluble BrC from each source is parameterized as a function of wavelength (Equation 11; Figure S10):

$$Ri \propto \lambda^{-w} \quad \text{(Equation 11)}$$

water-soluble BrC from fossil fuel combustion: $Ri = 4.568 \times 10^{10} \times \lambda^{-4.56}$
water-soluble BrC from biomass burning: $Ri = 3.491 \times 10^{12} \times \lambda^{-5.37}$
water-soluble BrC from BSOA: $Ri = 1.192 \times 10^{12} \times \lambda^{-5.49}$
water-soluble BrC from marine primary emissions: $Ri = 3.602 \times 10^{23} \times \lambda^{-10.1}$

We assumed the R_is of water-soluble BrC from each source in the upper air are the same as that measured at the surface, due to the lack of measurement in the upper air of the Arctic region. The optical property of BrC could be changing during advection and diffusion, which may lead to uncertainty in the estimation of BrC radiative forcing. However, the uncertainty is negligible based on the first measurement of altitude-resolved BrC in the United States with a variation of average MAE of BrC less than 0.4 from surface to upper air of ~12 km.[83] In addition, the simulated profiles of OC and BC using our model were evaluated in previous studies (Figure 2 of Samset et al.[84]; Figure S15 of Zhu et al.[82]). Overall, our model does a reasonable job of estimating BC concentrations at both high and low latitudes, so our model is reasonable to reproduce the vertically integrated radiative absorption of BrC.

The optical parameter of water-soluble BrC from each source was calculated based on the measurements in one season in a single year. By assuming that the optical property of WSOC from the certain source does not vary significantly, our method should be able to provide a relatively good estimate of the radiative absorption effect of WSOC in different years, even though the emission may vary. We summarized the MAE of BrC measured in previous studies in Figure S7 (also attached below), and the measured MAEs of BrC from the same source do not show a large difference. This assumption may introduce uncertainties in our estimation that would require more observations to be constrained in the Arctic region. We define the radiative absorption of water-soluble BrC as the difference in the net incoming radiation at the top of atmosphere between the InBrC and ExBrC schemes. The radiative effect (including absorption and scattering) of OC in the Arctic is calculated by the difference in the radiation at the top of atmosphere between with and without OC aerosols. The R_i of BC is constrained to 0.62 according to our measurement of BC optical properties, as stated above. The radiative effect of BC is defined by the difference in the radiation at the top of atmosphere between simulations with and without BC aerosols. Each model simulation was performed for 6 years of free running with the emission in 2015 from a Community Emissions Data System (CEDS) for CMIP6.[85] The later 5 years' data were used for analysis. We used 5 years of monthly average aerosol concentrations together with the first year of 4-hourly meteorological conditions to calculate the radiative effects. The model was run with winds nudged toward ECMWF reanalysis data using a nudging time of 6 h for the years 2017 and 1993 to evaluate the OC concentration in this circum-Arctic cruise and Alert site (Figure S11).

Molecular composition measured by FT-ICR MS

FT-ICR MS is a powerful platform for investigating the detailed characteristics of organic matter at the molecular level and has been applied to analyze chemical compositions in organic aerosols, cloud water, and aquatic environments.[54,86–88] This technique combines the advantages of ultrahigh resolution, sensitivity, and accuracy of mass measurements.[86] The analysis here is followed by the same procedure as in Xie et al.[87] Briefly, a portion of each sample (approximately 8 cm^2) was ultrasonicated three times for water-soluble extracts using Milli-Q water for 10 min. The combined extracts were acidified by HCl. This solution was then loaded onto a Solid Phase extraction cartridge (Oasis HLB, Waters, USA). To avoid incomplete elution, 12 mL of methanol was used to elute the cartridge. The resulting eluate was instantly concentrated on a rotary evaporator and then re-dissolved in 1 mL of methanol. The samples were analyzed in the negative ionization mode on an FT-ICR MS (Bruker Daltonik, Bremen, Germany; 7.0 T superconducting magnet with the solariX 2XR) with an electrospray ionization source. Samples were continuously injected at a flow rate of 180 μL h^{-1}. Mass spectra were collected over 256 scans with an ion accumulation time of 0.028 s. The mass limit was in the range m/z = 150–1,000 Da. The field blank was analyzed following the same procedure to detect possible contamination.

Molecular formula and peak intensity, a parameter interpreted as a proxy for concentration, of each molecule were measured by FT-ICR MS. FT-ICR MS peaks were considered if the signal-to-noise ratio was greater than six by allowing a mass error of 1.0 ppm between the theoretically calculated and the measured mass. Molecular formulae were assigned to peaks with elemental combinations up to 50 of ^{12}C, 100 of ^{1}H, 50 of ^{16}O, two of ^{14}N, and one of ^{32}S atoms.[89,90] Several rules were used to constrain the formula assignment, i.e., the elemental ratios of H/C < 2.5, O/C < 1.2, and S/C < 0.2, and the *N rule* for even electron ions.[91,92]

Molecules were categorized into eight structural classes according to the method by Bianco et al.[54] and Xie et al.[55] (criteria shown in Table S9) based on the elemental ratios H/C and O/C: lipid-like; aliphatic/peptide-like; carboxylic-rich alicyclic molecules-like/lignin-like; carbohydrate-like; unsaturated hydrocarbons; aromatic structures; highly oxygenated compounds/tannin-like; and other compounds.

Light absorption of individual molecules

Both the light absorption (b_{abs}) and molecules by FT-ICR MS were measured for the water extracts. Partial least-squares regression was used to estimate the light absorption of individual molecules following the method of Zeng et al.[50] The light absorption of water-soluble BrC (b_{abs}) is regressed on the measured peak intensity of each molecule. This regression derives an equivalent molecular absorption efficiency for each molecule. The contributions of each molecule to the light absorption of water-soluble BrC (b_{abs}) were calculated by using their equivalent molecular absorption efficiencies and their measured peak intensities. The light absorptions from the eight molecular classes were calculated by summing up the light absorption of the molecules included in each class.

The partial least-squares regression (PLSR) method was applied to estimate the contribution of the molecular compositions to the light absorption of water-soluble BrC ($b_{abs\text{-}365}$). The applicability of PLSR to apportion molecular contributions to the light absorption of BrC has been recently reported by Zeng et al.[50] Assuming that molecular absorption follows the Beer-Lambert law and a linear relationship of individual absorption of all molecules, the absorption (b_{abs}) of a sample would be the sum of the absorption from individual compounds with mass absorption coefficient ε and mass concentration c as $b_{abs,\,i} = \sum_{j=0}^{n}(\varepsilon_j \times c_{i,\,j})$, where i and j refer to the indices of a sample and a molecule, respectively. n represents the number of samples. For FT-ICR MS, the measured intensity of a molecule in a sample $I_{i,j}$ corresponds to its concentration multiplied by its ionization efficiency γ_j, as $I_{i,j} = c_{i,j} \times \gamma_j$. Thus, a linear relationship between the measured FT-ICR MS intensity I and b_{abs} can be formulated as $b_{abs,\,i} = \sum_{j=0}^{n}\left(\varepsilon_j \times I_{i,j}/\gamma_j\right) = \sum_{j=0}^{n}\left(\varepsilon_j/\gamma_j \times I_{i,j}\right) = \sum_{n=0}^{n}(\beta_j \times I_{i,\,j})$, where $\beta_j = \varepsilon_j/\gamma_j$, which is an equivalent molecular absorption

efficiency of an individual molecule. This integrated parameter reflects the absorption and ionization efficiency for individual molecules.

Here, we used the *pls* package (v.2.7-3)[93] in *R* language for PLSR analysis to retrieve β_i of individual molecules. PLSR is particularly suited when there are a large number of predictor variables with possible multicollinearity and relatively few samples.[93,94] PLSR combines the advantages of principal-component regression and multiple linear regression.[93,94] It can reduce the dimensions of the predicting variables (i.e., the measured intensity of molecules here) to derive new components. These components were used to model the measured data. Determining a practical number of components is an essential step for PLSR analysis. Increasing the number of components may reduce bias but will also increase error due to rising variance, causing an over-fit problem. Besides, cross-validation is usually used to evaluate the modeled apparent minimum overall error. Here, the leave-one-out cross-validation method was applied.

There are a large number of molecules detected (16,014) in all samples and a small number of common molecules (1,273; less than 10%). Using all the molecules in the PLSR will cause a large impact of the noise from molecules not detected in many samples, while using only the common molecules will potentially deteriorate the representation of the regression results. We sought a balance between PLSR modeling ability and the representation of molecules in samples. We first constructed a series of FT-ICR MS molecule datasets by considering a molecule's occurrence frequency in all samples. If a molecule occurred in at least $f_{molecule}$ (in percent) of the samples, it is included in a dataset, which is termed "$f_{molecule}$ dataset." $f_{molecule}$ ranges from 0% to 100% by a step of 5%. The 0% dataset represents a complete set of all molecules measured in any sample, while the 100% dataset only includes molecules that occurred in all samples, i.e., common molecules. Then, these datasets are used in the PLSR analysis on $b_{abs\text{-}365}$ individually. We evaluate the suitability of a dataset by the cross-validation R^2 (maximum among all number of components) in the cross-validation process for the regression on each dataset (Figure S15A). This is used to determine an FT-ICR MS dataset balancing the two influences as discussed at the start of this paragraph. As shown in Figure S15A, the cross-validation R^2 is around 0.35 for $f_{molecule}$ from 0% to 20%, while it reached to around 0.63 for a dataset containing only common molecules. When $f_{molecule}$ increased to 60%, the cross-validation R^2 reached around 0.55. We thus set $f_{molecule}$ to 60%, calling it the "$f_{molecule}$ = 60% dataset" (number of molecules: 4,330) and conducted the final regression on $b_{abs\text{-}365}$ on this dataset.

For this final regression, the optimal number of components is determined by examining the variation of both root-mean-squared error of prediction (RMSEP) and R^2 with the increasing number of components (i.e., latent variables, the terminology usually used in the PLSR field; Figures S15B and S15C). When RMSEP is the lowest and/or R^2 is the highest, it indicates a suitable number of components (here as four) to fit the model. In addition, the score plot (Figure S15D) shows that the fourth component can explain only 3.1% of the variation of $b_{abs\text{-}365}$. Thus, it is determined to use the three-component PLSR regression results, which are able to explain 81% of the variance of $b_{abs\text{-}365}$ (Figure S15E) and can avoid an over-fitting for the four-component solution. The equivalent molecular absorption efficiencies of each molecule are shown in Figure S15F for the three-component PLSR fitting. Ninety-six percent of the 4,330 molecules (n = 4,148) have non-negative equivalent molecular absorption efficiencies. A positive equivalent molecular absorption efficiency (the regressed coefficient, β) indicates the contribution of a molecule to the light absorption. Only 4.2% (n = 182) of the molecules had negative equivalent molecular absorption coefficients. These negative values might be caused by artifact statistical error[95] or self-association, causing a hypochromic effect.[96] In the following calculation, these small number of molecules with negative β values are removed because of the potential influence of the complicated interactions of chromophores.

Here, we focus on the light absorption contributed by individual molecules, molecular classes, and different sources, rather than on the component categorization resolved during the PLSR process. The light absorption by molecular structural classes is calculated by integrating the light absorption contributed by individual molecules in each class. This categorization method is suited to discuss the contribution of molecule structures and sources to the light absorption of water-soluble BrC.

Light absorption of water-insoluble BrC and total BrC. Water-insoluble fraction of organic carbon was extracted by methanol (HPLC grade) and filtered by polytetrafluoroethylene (PTFE) filters (SCBO-4542-1, PALL). The measurement of the light absorbance of water-insoluble BrC was measured by the ultraviolet-visible spectrophotometer (U3900H, Hitachi) as same for water-soluble BrC. Overall b_{abs} of water-insoluble BrC is calculated by the Equation 1, where WSOC is replaced by water-insoluble organic carbon (WIOC) ($WIOC = OC - WSOC$). The overall b_{abs} of total BrC was calculated as the sum of that of water-soluble and water-insoluble BrC. The MAE and the AAE (300–400 nm) of water-insoluble and total BrC were calculated by the Equations 2 and 3, respectively, where WSOC is replaced by WIOC and OC (a surrogate for total BrC). The overall b_{abs}, MAE, and AAE of water-insoluble and total BrC are shown in Table S2.

The source-apportionment of OC was additionally performed by the PMF model. The source-specific MAEs of total BrC were resolved via non-negative multivariate linear regression. The annual contributions of each source to the light absorption of total BrC in the Arctic were estimated based on the contribution of each source to OC concentration and the MAEs. These results are shown in Table S11.

SUPPLEMENTAL INFORMATION

Supplemental information can be found online at https://doi.org/10.1016/j.oneear.2022.02.006.

ACKNOWLEDGMENTS

We thank the researchers and the crew of *Xuelong* for their kind help for the sampling during the cruise. We acknowledge the use of data from NASA's Fire Information for Resource Management System (FIRMS) (https://earthdata.nasa.gov/firms), part of the NASA Earth Observing System Data and Information System (EOSDIS). We also thank Dr. Yuzhong Zhang from Westlake University for providing supporting information for this study. Y.C. and S.Y., etc., acknowledge the support from Max Planck Society (MPG) and the Minerva Program. This study was supported by the National Natural Science Foundation of China (grant no. 41625014 and no. 42177082).

AUTHOR CONTRIBUTIONS

S.Y., J.Z., P.F., and Y.C. designed the research. P.F. conceptualized the field campaign and provided logistical and financial support. W.L. collected the field samples. S.Y. conducted the measurement of WSOC and the light absorption of water-soluble BrC. S.C. measured the molecular composition by FT-ICR MS and pre-analyzed the data together with Q.X. H.R. and L.L. carried out the measurement of molecular tracers by GC/MS. S.S. measured ions. P.L. and H.M. measured the light absorption of water-insoluble BrC. Y.F. and B.C. measured OC and EC. S.Y. carried out the comprehensive analysis of the field data with inputs from other co-authors. J.Z. carried out the model simulations. S.Y. and J.Z. wrote the manuscript with specific inputs from Y.C., P.F., Q.X., M.O.A., and J.E.P. All co-authors commented on the manuscript.

DECLARATION OF INTERESTS

The authors declare no competing interests.

Received: July 29, 2021
Revised: January 23, 2022
Accepted: February 22, 2022
Published: March 18, 2022

REFERENCES

1. Graversen, R.G., Mauritsen, T., Tjernström, M., Källén, E., and Svensson, G. (2008). Vertical structure of recent Arctic warming. Nature *451*, 53–56. https://doi.org/10.1038/nature06502.
2. Ballinger, T.J., Overland, J.E., Wang, M., Bhatt, U.S., Hanna, E., Hanssen-Bauer, I., Kim, S.J., Thoman, R.L., and Walsh, J.E. (2020). Arctic Report

Card 2020: Surface Air Temperature (National Oceanic and Atmospheric Administration). https://doi.org/10.25923/gcw8-2z06.

3. Li, F., Wan, X., Wang, H., Orsolini, Y.J., Cong, Z., Gao, Y., and Kang, S. (2020). Arctic sea-ice loss intensifies aerosol transport to the Tibetan Plateau. Nat. Clim. Change *10*, 1037–1044. https://doi.org/10.1038/s41558-020-0881-2.
4. Oh, Y., Zhuang, Q., Liu, L., Welp, L.R., Lau, M.C.Y., Onstott, T.C., Medvigy, D., Bruhwiler, L., Dlugokencky, E.J., Hugelius, G., et al. (2020). Reduced net methane emissions due to microbial methane oxidation in a warmer Arctic. Nat. Clim. Change *10*, 317–321. https://doi.org/10.1038/s41558-020-0734-z.
5. Routson, C.C., McKay, N.P., Kaufman, D.S., Erb, M.P., Goosse, H., Shuman, B.N., Rodysill, J.R., and Ault, T. (2019). Mid-latitude net precipitation decreased with Arctic warming during the Holocene. Nature *568*, 83–87. https://doi.org/10.1038/s41586-019-1060-3.
6. Myers-Smith, I.H., Kerby, J.T., Phoenix, G.K., Bjerke, J.W., Epstein, H.E., Assmann, J.J., John, C., Andreu-Hayles, L., Angers-Blondin, S., Beck, P.S.A., et al. (2020). Complexity revealed in the greening of the Arctic. Nat. Clim. Change *10*, 106–117. https://doi.org/10.1038/s41558-019-0688-1.
7. Gautier, D.L., Bird, K.J., Charpentier, R.R., Grantz, A., Houseknecht, D.W., Klett, T.R., Moore, T.E., Pitman, J.K., Schenk, C.J., Schuenemeyer, J.H., et al. (2009). Assessment of undiscovered oil and gas in the Arctic. Science *324*, 1175–1179. https://doi.org/10.1126/science.1169467.
8. Sand, M., Berntsen, T.K., Von Salzen, K., Flanner, M.G., Langner, J., and Victor, D.G. (2016). Response of Arctic temperature to changes in emissions of short-lived climate forcers. Nat. Clim. Change *6*, 286. https://doi.org/10.1038/Nclimate2880.
9. Zhang, X., Chen, S., Kang, L., Yuan, T., Luo, Y., Alam, K., Li, J., He, Y., Bi, H., and Zhao, D. (2020). Direct radiative forcing induced by light-absorbing aerosols in different climate regions over East Asia. J. Geophys. Res. Atmos. *125*. e2019JD032228. https://doi.org/10.1029/2019jd032228.
10. Oshima, N., Yukimoto, S., Deushi, M., Koshiro, T., Kawai, H., Tanaka, T.Y., and Yoshida, K. (2020). Global and Arctic effective radiative forcing of anthropogenic gases and aerosols in MRI-ESM2.0. Prog. Earth Planet. Sci. *7*, 38. https://doi.org/10.1186/s40645-020-00348-w.
11. Zeng, L., Zhang, A., Wang, Y., Wagner, N.L., Katich, J.M., Schwarz, J.P., Schill, G.P., Brock, C., Froyd, K.D., Murphy, D.M., et al. (2020). Global measurements of brown carbon and estimated direct radiative effects. Geophys. Res. Lett. *47*. e2020GL088747. https://doi.org/10.1029/2020GL088747.
12. Yue, S., Bikkina, S., Gao, M., Barrie, L.A., Kawamura, K., and Fu, P. (2019). Sources and radiative absorption of water-soluble brown carbon in the high Arctic atmosphere. Geophys. Res. Lett. *46*, 14881–14891. https://doi.org/10.1029/2019GL085318.
13. Corr, C.A., Hall, S.R., Ullmann, K., Anderson, B.E., Beyersdorf, A.J., Thornhill, K.L., Cubison, M.J., Jimenez, J.L., Wisthaler, A., and Dibb, J.E. (2012). Spectral absorption of biomass burning aerosol determined from retrieved single scattering albedo during ARCTAS. Atmos. Chem. Phys. *12*, 10505–10518. https://doi.org/10.5194/acp-12-10505-2012.
14. June, N.A., Wang, X., Chen, L.W.A., Chow, J.C., Watson, J.G., Wang, X., Henderson, B.H., Zheng, Y., and Mao, J. (2020). Spatial and temporal variability of brown carbon in the United States: implications for direct radiative effects. Geophys. Res. Lett. *47*. e2020GL090332. https://doi.org/10.1029/2020gl090332.
15. Evangeliou, N., Kylling, A., Eckhardt, S., Myroniuk, V., Stebel, K., Paugam, R., Zibtsev, S., and Stohl, A. (2019). Open fires in Greenland in summer 2017: transport, deposition and radiative effects of BC, OC and BrC emissions. Atmos. Chem. Phys. *19*, 1393–1411. https://doi.org/10.5194/acp-19-1393-2019.
16. Sand, M., Samset, B.H., Balkanski, Y., Bauer, S., Bellouin, N., Berntsen, T.K., Bian, H., Chin, M., Diehl, T., Easter, R., et al. (2017). Aerosols at the poles: an AeroCom phase II multi-model evaluation. Atmos. Chem. Phys. *17*, 12197–12218. https://doi.org/10.5194/acp-17-12197-2017.
17. Zhang, A.X., Wang, Y.H., Zhang, Y.Z., Weber, R.J., Song, Y.J., Ke, Z.M., and Zou, Y.F. (2020). Modeling the global radiative effect of brown carbon: a potentially larger heating source in the tropical free troposphere than black carbon. Atmos. Chem. Phys. *20*, 1901–1920. https://doi.org/10.5194/acp-20-1901-2020.
18. Lack, D.A., Langridge, J.M., Bahreini, R., Cappa, C.D., Middlebrook, A.M., and Schwarz, J.P. (2012). Brown carbon and internal mixing in biomass burning particles. Proc. Nat. Acad. Sci. U S A *109*, 14802–14807. https://doi.org/10.1073/pnas.1206575109.
19. Selimovic, V., Yokelson, R.J., McMeeking, G.R., and Coefield, S. (2019). In situ measurements of trace gases, PM, and aerosol optical properties during the 2017 NW US wildfire smoke event. Atmos. Chem. Phys. *19*, 3905–3926. https://doi.org/10.5194/acp-19-3905-2019.
20. Selimovic, V., Yokelson, R.J., Warneke, C., Roberts, J.M., de Gouw, J., Reardon, J., and Griffith, D.W.T. (2018). Aerosol optical properties and trace gas emissions by PAX and OP-FTIR for laboratory-simulated western US wildfires during FIREX. Atmos. Chem. Phys. *18*, 2929–2948. https://doi.org/10.5194/acp-18-2929-2018.
21. Kasischke, E.S., and Turetsky, M.R. (2006). Recent changes in the fire regime across the North American boreal region—spatial and temporal patterns of burning across Canada and Alaska. Geophys. Res. Lett. *33*, L09703. https://doi.org/10.1029/2006GL025677.
22. Walker, X.J., Baltzer, J.L., Cumming, S.G., Day, N.J., Ebert, C., Goetz, S., Johnstone, J.F., Potter, S., Rogers, B.M., Schuur, E.A.G., et al. (2019). Increasing wildfires threaten historic carbon sink of boreal forest soils. Nature *572*, 520–523. https://doi.org/10.1038/s41586-019-1474-y.
23. Konovalov, I.B., Lvova, D.A., Beekmann, M., Jethva, H., Mikhailov, E.F., Paris, J.D., Belan, B.D., Kozlov, V.S., Ciais, P., and Andreae, M.O. (2018). Estimation of black carbon emissions from Siberian fires using satellite observations of absorption and extinction optical depths. Atmos. Chem. Phys. *18*, 14889–14924. https://doi.org/10.5194/acp-18-14889-2018.
24. Buixadé Farré, A., Stephenson, S.R., Chen, L., Czub, M., Dai, Y., Demchev, D., Efimov, Y., Graczyk, P., Grythe, H., Keil, K., et al. (2014). Commercial Arctic shipping through the Northeast Passage: routes, resources, governance, technology, and infrastructure. Polar. Geogr. *37*, 298–324. https://doi.org/10.1080/1088937X.2014.965769.
25. Petäjä, T., Duplissy, E.M., Tabakova, K., Schmale, J., Altstädter, B., Ancellet, G., Arshinov, M., Balin, Y., Baltensperger, U., Bange, J., et al. (2020). Overview: integrative and comprehensive understanding on polar environments (iCUPE) – concept and initial results. Atmos. Chem. Phys. *20*, 8551–8592. https://doi.org/10.5194/acp-20-8551-2020.
26. Yu, H., Li, W., Zhang, Y., Tunved, P., Dall'Osto, M., Shen, X., Sun, J., Zhang, X., Zhang, J., and Shi, Z. (2019). Organic coating on sulfate and soot particles during late summer in the Svalbard Archipelago. Atmos. Chem. Phys. *19*, 10433–10446. https://doi.org/10.5194/acp-19-10433-2019.
27. Shantz, N.C., Gultepe, I., Andrews, E., Zelenyuk, A., Earle, M.E., Macdonald, A.M., Liu, P.S.K., and Leaitch, W.R. (2014). Optical, physical, and chemical properties of springtime aerosol over Barrow Alaska in 2008. Int. J. Climatol. *34*, 3125–3138. https://doi.org/10.1002/joc.3898.
28. Xie, Y., Li, Z., Li, L., Wagener, R., Abboud, I., Li, K., Li, D., Zhang, Y., Chen, X., and Xu, H. (2018). Aerosol optical, microphysical, chemical and radiative properties of high aerosol load cases over the Arctic based on AERONET measurements. Sci. Rep. *8*, 9376. https://doi.org/10.1038/s41598-018-27744-z.
29. McNaughton, C.S., Clarke, A.D., Freitag, S., Kapustin, V.N., Kondo, Y., Moteki, N., et al. (2011). Absorbing aerosol in the troposphere of the Western Arctic during the 2008 ARCTAS/ARCPAC airborne field campaigns. Atmos. Chem. Phys. *11*, 7561–7582. https://doi.org/10.5194/acp-11-7561-2011.
30. Wang, X., Heald, C.L., Ridley, D.A., Schwarz, J.P., Spackman, J.R., Perring, A.E., Coe, H., Liu, D., and Clarke, A.D. (2014). Exploiting simultaneous observational constraints on mass and absorption to estimate the global direct radiative forcing of black carbon and brown carbon. Atmos. Chem. Phys. *14*, 10989–11010. https://doi.org/10.5194/acp-14-10989-2014.
31. Lin, G., Penner, J.E., Flanner, M.G., Sillman, S., Xu, L., and Zhou, C. (2014). Radiative forcing of organic aerosol in the atmosphere and on snow:

effects of SOA and brown carbon. J. Geophys. Res. Atmos. *119*, 7453–7476. https://doi.org/10.1002/2013jd021186.

32. Saleh, R., Marks, M., Heo, J., Adams, P.J., Donahue, N.M., and Robinson, A.L. (2015). Contribution of brown carbon and lensing to the direct radiative effect of carbonaceous aerosols from biomass and biofuel burning emissions. J. Geophys. Res. Atmos. *120*, 10285–10296. https://doi.org/10.1002/2015jd023697.

33. Wang, X., Heald, C.L., Liu, J., Weber, R.J., Campuzano-Jost, P., Jimenez, J.L., Schwarz, J.P., and Perring, A.E. (2018). Exploring the observational constraints on the simulation of brown carbon. Atmos. Chem. Phys. *18*, 635–653. https://doi.org/10.5194/acp-18-635-2018.

34. Brown, H., Liu, X., Feng, Y., Jiang, Y., Wu, M., Lu, Z., Wu, C., Murphy, S., and Pokhrel, R. (2018). Radiative effect and climate impacts of brown carbon with the Community Atmosphere Model (CAM5). Atmos. Chem. Phys. *18*, 17745–17768. https://doi.org/10.5194/acp-18-17745-2018.

35. Barrett, T.E., and Sheesley, R.J. (2017). Year-round optical properties and source characterization of Arctic organic carbon aerosols on the North Slope Alaska. J. Geophys. Res. Atmos. *122*, 9319–9331. https://doi.org/10.1002/2016jd026194.

36. Huang, R.-J., Yang, L., Cao, J.-j., Chen, Y., Chen, Q., Li, Y., Duan, J., Zhu, C., Dai, W., Wang, K., et al. (2018). Brown carbon aerosol in urban Xi'an, northwest China: the composition and light absorption properties. Environ. Sci. Technol. *52*, 6825–6833. https://doi.org/10.1021/acs.est.8b02386.

37. Srinivas, B., Rastogi, N., Sarin, M.M., Singh, A., and Singh, D. (2016). Mass absorption efficiency of light absorbing organic aerosols from source region of paddy-residue burning emissions in the Indo-Gangetic Plain. Atmos. Environ. *125*, 360–370. https://doi.org/10.1016/j.atmosenv.2015.07.017.

38. Schlitzer, R. (2021). Ocean Data View. https://odv.awi.de.

39. Laskin, A., Laskin, J., and Nizkorodov, S.A. (2015). Chemistry of atmospheric brown carbon. Chem. Rev. *115*, 4335–4382. https://doi.org/10.1021/cr5006167.

40. Zhu, C.-S., Zhang, Z.-S., Tao, J., Qu, Y., and Cao, J.-J. (2020). Indication of primary biogenic contribution to BrC over a high altitude location in the southeastern Tibet. Atmos. Environ. *231*, 117462. https://doi.org/10.1016/j.atmosenv.2020.117462.

41. Moise, T., Flores, J.M., and Rudich, Y. (2015). Optical properties of secondary organic aerosols and their changes by chemical processes. Chem. Rev. *115*, 4400–4439. https://doi.org/10.1021/cr5005259.

42. Abbatt, J.P.D., Leaitch, W.R., Aliabadi, A.A., Bertram, A.K., Blanchet, J.P., Boivin-Rioux, A., Bozem, H., Burkart, J., Chang, R.Y.W., Charette, J., et al. (2019). Overview paper: new insights into aerosol and climate in the Arctic. Atmos. Chem. Phys. *19*, 2527–2560. https://doi.org/10.5194/acp-19-2527-2019.

43. Kirillova, E.N., Andersson, A., Han, J., Lee, M., and Gustafsson, Ö. (2014). Sources and light absorption of water-soluble organic carbon aerosols in the outflow from northern China. Atmos. Chem. Phys. *14*, 1413–1422. https://doi.org/10.5194/acp-14-1413-2014.

44. Kirillova, E.N., Marinoni, A., Bonasoni, P., Vuillermoz, E., Facchini, M.C., Fuzzi, S., and Decesari, S. (2016). Light absorption properties of brown carbon in the high Himalayas. J. Geophys. Res. Atmos. *121*, 9621–9639. https://doi.org/10.1002/2016jd025030.

45. Kirillova, E.N., Andersson, A., Tiwari, S., Srivastava, A.K., Bisht, D.S., and Gustafsson, Ö. (2014). Water-soluble organic carbon aerosols during a full New Delhi winter: isotope-based source apportionment and optical properties. J. Geophys. Res. Atmos. *119*, 3476–3485. https://doi.org/10.1002/2013jd020041.

46. Pistone, K., Eisenman, I., and Ramanathan, V. (2014). Observational determination of albedo decrease caused by vanishing Arctic sea ice. Proc. Nat. Acad. Sci. USA *111*, 3322–3326. https://doi.org/10.1073/pnas.1318201111.

47. Doherty, S.J., Warren, S.G., Grenfell, T.C., Clarke, A.D., and Brandt, R.E. (2010). Light-absorbing impurities in Arctic snow. Atmos. Chem. Phys. *10*, 11647–11680. https://doi.org/10.5194/acp-10-11647-2010.

48. Skiles, S.M., Flanner, M., Cook, J.M., Dumont, M., and Painter, T.H. (2018). Radiative forcing by light-absorbing particles in snow. Nat. Clim. Change *8*, 964–971. https://doi.org/10.1038/s41558-018-0296-5.

49. Tuccella, P., Pitari, G., Colaiuda, V., Raparelli, E., and Curci, G. (2021). Present-day radiative effect from radiation-absorbing aerosols in snow. Atmos. Chem. Phys. *21*, 6875–6893. https://doi.org/10.5194/acp-21-6875-2021.

50. Zeng, Y., Shen, Z., Takahama, S., Zhang, L., Zhang, T., Lei, Y., Zhang, Q., Xu, H., Ning, Y., Huang, Y., et al. (2020). Molecular absorption and evolution mechanisms of PM2.5 brown carbon revealed by electrospray ionization Fourier transform–ion cyclotron resonance mass spectrometry during a severe winter pollution episode in Xi'an, China. Geophys. Res. Lett. *47*. e2020GL087977. https://doi.org/10.1029/2020GL087977.

51. Nozière, B., Kalberer, M., Claeys, M., Allan, J., D'Anna, B., Decesari, S., Finessi, E., Glasius, M., Grgić, I., Hamilton, J.F., et al. (2015). The molecular identification of organic compounds in the atmosphere: state of the art and challenges. Chem. Rev. *115*, 3919–3983. https://doi.org/10.1021/cr5003485.

52. Tang, J., Li, J., Su, T., Han, Y., Mo, Y., Jiang, H., Cui, M., Jiang, B., Chen, Y., Tang, J., et al. (2020). Molecular compositions and optical properties of dissolved brown carbon in biomass burning, coal combustion, and vehicle emission aerosols illuminated by excitation–emission matrix spectroscopy and Fourier transform ion cyclotron resonance mass spectrometry analysis. Atmos. Chem. Phys. *20*, 2513–2532. https://doi.org/10.5194/acp-20-2513-2020.

53. Kroll, J.H., Donahue, N.M., Jimenez, J.L., Kessler, S.H., Canagaratna, M.R., Wilson, K.R., Altieri, K.E., Mazzoleni, L.R., Wozniak, A.S., Bluhm, H., et al. (2011). Carbon oxidation state as a metric for describing the chemistry of atmospheric organic aerosol. Nat. Chem. *3*, 133–139. https://doi.org/10.1038/nchem.948.

54. Bianco, A., Deguillaume, L., Vaitilingom, M., Nicol, E., Baray, J.L., Chaumerliac, N., and Bridoux, M. (2018). Molecular characterization of cloud water samples collected at the puy de Dôme (France) by Fourier transform ion cyclotron resonance mass spectrometry. Environ. Sci. Technol. *52*, 10275–10285. https://doi.org/10.1021/acs.est.8b01964.

55. Xie, Q., Su, S., Chen, S., Zhang, Q., Yue, S., Zhao, W., Du, H., Ren, H., Wei, L., Cao, D., et al. (2021). Molecular characterization of size-segregated organic aerosols in the urban boundary layer in wintertime Beijing by FT-ICR MS. Faraday Discuss. *226*, 457–478. https://doi.org/10.1039/D0FD00084A.

56. Higuera, P.E., Shuman, B.N., and Wolf, K.D. (2021). Rocky Mountain subalpine forests now burning more than any time in recent millennia. Proc. Nat. Acad. Sci. USA *118*. e2103135118. https://doi.org/10.1073/pnas.2103135118.

57. Moritz, M.A., Batllori, E., Bradstock, R.A., Gill, A.M., Handmer, J., Hessburg, P.F., Leonard, J., McCaffrey, S., Odion, D.C., Schoennagel, T., and Syphard, A.D. (2014). Learning to coexist with wildfire. Nature *515*, 58–66. https://doi.org/10.1038/nature13946.

58. Westerling, A.L. (2016). Increasing western US forest wildfire activity: sensitivity to changes in the timing of spring. Philos. Trans. R. Soc. B Biol. Sci. *371*, 20150178. https://doi.org/10.1098/rstb.2015.0178.

59. Westerling, A.L., Hidalgo, H.G., Cayan, D.R., and Swetnam, T.W. (2006). Warming and earlier spring increase western U.S. Forest wildfire activity. Science *313*, 940–943. https://doi.org/10.1126/science.1128834.

60. Winiger, P., Barrett, T.E., Sheesley, R.J., Huang, L., Sharma, S., Barrie, L.A., Yttri, K.E., Evangeliou, N., Eckhardt, S., Stohl, A., et al. (2019). Source apportionment of circum-Arctic atmospheric black carbon from isotopes and modeling. Sci. Adv. *5*, eaau8052. https://doi.org/10.1126/sciadv.aau8052.

61. Stein, A.F., Draxler, R.R., Rolph, G.D., Stunder, B.J.B., Cohen, M.D., and Ngan, F. (2015). NOAA's HYSPLIT atmospheric transport and dispersion modeling system. Bull. Am. Meteorol. Soc. *96*, 2059–2077. https://doi.org/10.1175/BAMS-D-14-00110.1.

62. Hecobian, A., Zhang, X., Zheng, M., Frank, N., Edgerton, E.S., and Weber, R.J. (2010). Water-soluble organic aerosol material and the light-absorption characteristics of aqueous extracts measured over the southeastern United States. Atmos. Chem. Phys. *10*, 5965–5977. https://doi.org/10.5194/acp-10-5965-2010.

63. Srinivas, B., and Sarin, M.M. (2013). Light absorbing organic aerosols (brown carbon) over the tropical Indian Ocean: impact of biomass burning emissions. Environ. Res. Lett. *8*, 44042. https://doi.org/10.1088/1748-9326/8/4/044042.

64. Fu, P., Kawamura, K., Okuzawa, K., Aggarwal, S.G., Wang, G., Kanaya, Y., and Wang, Z. (2008). Organic molecular compositions and temporal variations of summertime mountain aerosols over Mt. Tai, North China Plain. J. Geophys. Res. Atmos. *113*, D19107. https://doi.org/10.1029/2008jd009900.

65. Schauer, J.J., Rogge, W.F., Hildemann, L.M., Mazurek, M.A., Cass, G.R., and Simoneit, B.R.T. (1996). Source apportionment of airborne particulate matter using organic compounds as tracers. Atmos. Environ. *30*, 3837–3855. https://doi.org/10.1016/1352-2310(96)00085-4.

66. Brown, S.G., Eberly, S., Paatero, P., and Norris, G.A. (2015). Methods for estimating uncertainty in PMF solutions: examples with ambient air and water quality data and guidance on reporting PMF results. Sci. Total Environ. *518*, 626–635. https://doi.org/10.1016/j.scitotenv.2015.01.022.

67. Geng, X., Mo, Y., Li, J., Zhong, G., Tang, J., Jiang, H., Ding, X., Malik, R.N., and Zhang, G. (2020). Source apportionment of water-soluble brown carbon in aerosols over the northern South China Sea: influence from land outflow, SOA formation and marine emission. Atmos. Environ. *229*, 117484. https://doi.org/10.1016/j.atmosenv.2020.117484.

68. Wang, Q., He, X., Huang, X.H.H., Griffith, S.M., Feng, Y., Zhang, T., Zhang, Q., Wu, D., and Yu, J.Z. (2017). Impact of secondary organic aerosol tracers on tracer-based source apportionment of organic carbon and PM2.5: a case study in the Pearl River Delta, China. ACS Earth Space Chem. *1*, 562–571. https://doi.org/10.1021/acsearthspacechem.7b00088.

69. Paatero, P., Eberly, S., Brown, S.G., and Norris, G.A. (2014). Methods for estimating uncertainty in factor analytic solutions. Atmos. Meas. Tech. *7*, 781–797. https://doi.org/10.5194/amt-7-781-2014.

70. Liu, J., Bergin, M., Guo, H., King, L., Kotra, N., Edgerton, E., and Weber, R.J. (2013). Size-resolved measurements of brown carbon in water and methanol extracts and estimates of their contribution to ambient fine-particle light absorption. Atmos. Chem. Phys. *13*, 12389–12404. https://doi.org/10.5194/acp-13-12389-2013.

71. Ammerlaan, B.A.J., Holzinger, R., Jedynska, A.D., and Henzing, J.S. (2017). Technical note: aerosol light absorption measurements with a carbon analyser – calibration and precision estimates. Atmos. Environ. *164*, 1–7. https://doi.org/10.1016/j.atmosenv.2017.05.031.

72. Ram, K., and Sarin, M. (2009). Absorption coefficient and site-specific mass absorption efficiency of elemental carbon in aerosols over urban, rural, and high-altitude sites in India. Environ. Sci. Technol. *43*, 8233–8239. https://doi.org/10.1021/es9011542.

73. Willis, M.D., Leaitch, W.R., and Abbatt, J.P.D. (2018). Processes controlling the composition and abundance of Arctic aerosol. Rev. Geophys. *56*, 621–671. https://doi.org/10.1029/2018rg000602.

74. Weingartner, E., Saathoff, H., Schnaiter, M., Streit, N., Bitnar, B., and Baltensperger, U. (2003). Absorption of light by soot particles: determination of the absorption coefficient by means of aethalometers. J. Aerosol. Sci. *34*, 1445–1463. https://doi.org/10.1016/S0021-8502(03)00359-8.

75. Bond, T.C., and Bergstrom, R.W. (2006). Light absorption by carbonaceous particles: an investigative review. Aerosol Sci. Technol. *40*, 27–67. https://doi.org/10.1080/02786820500421521.

76. Liu, F., Yon, J., Fuentes, A., Lobo, P., Smallwood, G.J., and Corbin, J.C. (2020). Review of recent literature on the light absorption properties of black carbon: refractive index, mass absorption cross section, and absorption function. Aerosol Sci. Technol. *54*, 33–51. https://doi.org/10.1080/02786826.2019.1676878.

77. Chung, C.E., Lee, K., and Müller, D. (2011). Effect of internal mixture on black carbon radiative forcing. Tellus B *64*, 10925. https://doi.org/10.3402/tellusb.v64i0.10925.

78. Zhu, J., Penner, J.E., Lin, G., Zhou, C., Xu, L., and Zhuang, B. (2017). Mechanism of SOA formation determines magnitude of radiative effects. Proc. Nat. Acad. Sci. USA *114*, 12685–12690. https://doi.org/10.1073/pnas.1712273114.

79. Zhu, J., and Penner, J.E. (2019). Global modeling of secondary organic aerosol with organic nucleation. J. Geophys. Res. Atmos. *124*, 8260–8286. https://doi.org/10.1029/2019jd030414.

80. Zhu, J., and Penner, J.E. (2020). Indirect effects of secondary organic aerosol on cirrus clouds. J. Geophys. Res. Atmos. *125*. e2019JD032233. https://doi.org/10.1029/2019jd032233.

81. Fu, P., Kawamura, K., and Barrie, L.A. (2009). Photochemical and other sources of organic compounds in the Canadian high Arctic aerosol pollution during winter-spring. Environ. Sci. Technol. *43*, 286–292. https://doi.org/10.1021/es803046q.

82. Zhu, J., Penner, J.E., Yu, F., Sillman, S., Andreae, M.O., and Coe, H. (2019). Decrease in radiative forcing by organic aerosol nucleation, climate, and land use change. Nat. Commun. *10*, 423. https://doi.org/10.1038/s41467-019-08407-7.

83. Zhang, Y., Forrister, H., Liu, J., Dibb, J., Anderson, B., Schwarz, J.P., Perring, A.E., Jimenez, J.L., Campuzano-Jost, P., Wang, Y., et al. (2017). Top-of-atmosphere radiative forcing affected by brown carbon in the upper troposphere. Nat. Geosci. *10*, 486. https://doi.org/10.1038/ngeo2960.

84. Samset, B.H., Myhre, G., Herber, A., Kondo, Y., Li, S.M., Moteki, N., Koike, M., Oshima, N., Schwarz, J.P., Balkanski, Y., et al. (2014). Modelled black carbon radiative forcing and atmospheric lifetime in AeroCom Phase II constrained by aircraft observations. Atmos. Chem. Phys. *14*, 12465–12477. https://doi.org/10.5194/acp-14-12465-2014.

85. Hoesly, R.M., Smith, S.J., Feng, L., Klimont, Z., Janssens-Maenhout, G., Pitkanen, T., Seibert, J.J., Vu, L., Andres, R.J., Bolt, R.M., et al. (2018). Historical (1750–2014) anthropogenic emissions of reactive gases and aerosols from the Community Emissions Data System (CEDS). Geosci. Model. Dev. *11*, 369–408. https://doi.org/10.5194/gmd-11-369-2018.

86. Kellerman, A.M., Kothawala, D.N., Dittmar, T., and Tranvik, L.J. (2015). Persistence of dissolved organic matter in lakes related to its molecular characteristics. Nat. Geosci. *8*, 454. https://doi.org/10.1038/ngeo2440.

87. Xie, Q., Li, Y., Yue, S., Su, S., Cao, D., Xu, Y., Chen, J., Tong, H., Su, H., Cheng, Y., et al. (2020). Increase of high molecular weight organosulfate with intensifying urban air pollution in the megacity Beijing. J. Geophys. Res. Atmos. *125*. e2019JD032200. https://doi.org/10.1029/2019JD032200.

88. Lin, P., Rincon, A.G., Kalberer, M., and Yu, J.Z. (2012). Elemental composition of HULIS in the Pearl river Delta region, China: results inferred from positive and negative electrospray high resolution mass spectrometric data. Environ. Sci. Technol. *46*, 7454–7462. https://doi.org/10.1021/es300285d.

89. Cao, D., Lv, J., Geng, F., Rao, Z., Niu, H., Shi, Y., Cai, Y., and Kang, Y. (2016). Ion accumulation time dependent molecular characterization of natural organic matter using electrospray ionization-Fourier transform ion cyclotron resonance mass spectrometry. Anal. Chem. *88*, 12210–12218. https://doi.org/10.1021/acs.analchem.6b03198.

90. Mazzoleni, L.R., Saranjampour, P., Dalbec, M.M., Samburova, V., Hallar, A.G., Zielinska, B., Lowenthal, D.H., and Kohl, S. (2012). Identification of water-soluble organic carbon in non-urban aerosols using ultrahigh-resolution FT-ICR mass spectrometry: organic anions. Environ. Chem. *9*, 285–297. https://doi.org/10.1071/En11167.

91. Wozniak, A.S., Bauer, J.E., Sleighter, R.L., Dickhut, R.M., and Hatcher, P.G. (2008). Technical Note: molecular characterization of aerosol-derived water soluble organic carbon using ultrahigh resolution electrospray ionization Fourier transform ion cyclotron resonance mass spectrometry. Atmos. Chem. Phys. *8*, 5099–5111. https://doi.org/10.5194/acp-8-5099-2008.

92. Zhang, L., Wang, S., Xu, Y., Shi, Q., Zhao, H., Jiang, B., and Yang, J. (2016). Molecular characterization of lake sediment WEON by Fourier transform ion cyclotron resonance mass spectrometry and its environmental implications. Water Res. *106*, 196–203. https://doi.org/10.1016/j.watres.2016.09.059.

93. Mevik, B.H., and Wehrens, R. (2007). The pls package: principal component and partial least squares regression in R. J. Stat. Softw. *18*, 1–23. https://doi.org/10.18637/jss.v018.i02.

94. Wold, S., Ruhe, A., Wold, H., and Dunn, I.W. (1984). The collinearity problem in linear regression. The partial least squares (PLS) approach to generalized inverses. SIAM J. Sci. Stat. Comput. *5*, 735–743. https://doi.org/10.1137/0905052.

95. Cramer, R.D. (1993). Partial least squares (PLS): its strengths and limitations. Perspect. Drug Discov. Des. *1*, 269–278. https://doi.org/10.1007/BF02174528.

96. Peral, F., and Gallego, E. (2000). Self-association of pyridine-2,6-dicarboxylic acid in aqueous solution as determined from ultraviolet hypochromic and hyperchromic effects. Spectrochim. Acta A Mol. Biomol. Spectrosc. *56*, 2149–2155. https://doi.org/10.1016/S1386-1425(00)00270-5.

One Earth, Volume *5*

Supplemental information

Brown carbon from biomass burning imposes strong circum-Arctic warming

Siyao Yue, Jialei Zhu, Shuang Chen, Qiaorong Xie, Wei Li, Linjie Li, Hong Ren, Sihui Su, Ping Li, Hao Ma, Yanbing Fan, Borong Cheng, Libin Wu, Junjun Deng, Wei Hu, Lujie Ren, Lianfang Wei, Wanyu Zhao, Yu Tian, Xiaole Pan, Yele Sun, Zifa Wang, Fengchang Wu, Cong-Qiang Liu, Hang Su, Joyce E. Penner, Ulrich Pöschl, Meinrat O. Andreae, Yafang Cheng, and Pingqing Fu

Table S1. Marine aerosol sampling information during the 2017 circum-Arctic cruise of the Research Vessel *Xuelong*.

Sample ID	Start Time (UTC)	Volume (m^3)
BJ17-6	7/30/17 7:20	2880
BJ17-7	8/1/17 7:20	2880
BJ17-8	8/3/17 7:20	2880
BJ17-9	8/5/17 7:20	2880
BJ17-10	8/7/17 7:25	2880
BJ17-11	8/9/17 7:17	2880
BJ17-12	8/11/17 7:18	2880
BJ17-13	8/13/17 7:20	2880
BJ17-14	8/15/17 7:20	2880
BJ17-15	8/17/17 7:20	2880
BJ17-16	8/19/17 7:22	2880
BJ17-17	8/21/17 7:16	2880
BJ17-18	8/23/17 7:12	2880
BJ17-19	8/25/17 11:31	2880
BJ17-20	8/27/17 11:40	618
BJ17-21	9/5/17 13:00	2880
BJ17-22	9/7/17 13:05	2880
BJ17-23	9/10/17 0:05	2880
BJ17-24	9/12/17 0:11	2880
BJ17-25	9/14/17 0:11	2880
BJ17-26	9/16/17 0:10	2880
BJ17-27	9/18/17 0:10	2880
BJ17-28	9/20/17 0:00	2880
BJ17-29	9/22/17 0:03	2880
BJ17-30	9/24/17 0:03	2880

Table S2. Statistics of the concentrations of carbonaceous species, light absorption properties of BrC in the circum-Arctic.

Parameter	Average ± Standard deviation	Range
OC (μgC m^{-3})	0.63 ± 0.42	0.12–1.9
EC (ngC m^{-3})	63 ± 67	0–284
WSOC (μgC m^{-3})	0.21 ± 0.15	0.07–0.74
WIOC (μgC m^{-3})	0.42 ± 0.39	0.02–1.6
WSOC/OC (%)	41 ± 25	10–89
WIOC/OC (%)	59 ± 25	11–90
Light absorption properties of water-soluble BrC		
$b_{abs\text{-}365}$ (M m^{-1})	0.10 ± 0.05	0.02–0.26
MAE_{365} (m^2 g^{-1})	0.56 ± 0.30	0.17–1.2
AAE_{BrC} (300–400 nm)	6.8 ± 0.98	5.7–8.8
Light absorption properties of water-insoluble BrC		
$b_{abs\text{-}365}$ (M m^{-1})	0.08 ± 0.04	0.02–0.16
MAE_{365} (m^2 g^{-1})	0.30 ± 0.26	0.08–1.2
AAE_{BrC} (300–400 nm)	5.8 ± 1.0	3.2–7.9
Light absorption properties of total BrC		
$b_{abs\text{-}365}$ (M m^{-1})	0.17 ± 0.08	0.03–0.42
MAE_{365} (m^2 g^{-1})	0.31 ± 0.11	0.13–0.72
AAE_{BrC} (300–400 nm)	5.9 ± 0.76	4.1–6.9
$b_{abs\text{-}365}$ ratio (water-insoluble / water-soluble) (%)	81 ± 38	29–179

Table S3. Tracers used to identify the sources resolved by positive matrix factorization.

Tracers	Sources	References
WSOC	multiple sources	[1]
chloride	sea spray emission	[2]
sulfate	sea spray emission, secondary oxidation	[3]
sodium	sea spray emission	[2]
MSA	oxidation products of dimethyl sulfide emitted by ocean biomass	[3,4]
sucrose	pollen	[5]
arabitol	fungal spores	[6]
trehalose	soil dust	[7]
glucose	vegetation (e.g., trees, branches, leaves)	[5]
2-MGA	photooxidation, isoprene derived SOA	[8,9]
pinic acid	photooxidation, monoterpene derived SOA	[10]
EC	fossil fuel combustion, biomass burning	[11]
levoglucosan	biomass burning	[12]
mannosan	biomass burning	[12]
hopane $C_{29}\alpha\beta$	petroleum and coal combustion	[13]
BeP	fossil fuel combustion, biomass burning	[14]

Table S4. Constraints of the chemical species in the factor profiles in positive matrix factorization analysis. Here, "–" indicates no constraints were applied, while "0" indicates a zero-contribution of a species to a factor.

Species	Marine secondary aerosol	Biomass burning	FF-1	BSOA	Bioaerosol	Primary micro-organism / plankton	FF-2	Marine primary emission
WSOC	–	–	–	–	–	–	–	–
chloride	–	–	–	–	–	–	–	–
sulfate	–	–	–	–	–	–	–	–
sodium	–	–	–	–	–	–	–	–
MSA	–	–	–	–	–	–	–	–
sucrose	–	–	–	–	–	–	–	–
arabitol	–	–	–	–	–	–	–	–
trehalose	–	–	–	–	–	–	–	–
glucose	–	–	–	–	–	–	–	–
2-MGA	–	–	0	–	–	–	0	–
pinic acid	–	–	0	–	–	–	0	–
EC	0	–	–	0	0	0	–	0
levoglucosan	0	–	0	0	0	0	0	0
mannosan	0	–	0	0	0	0	0	0
hopane $C_{29}\alpha\beta$	0	–	–	0	0	0	–	0
BeP	–	–	–	–	–	–	–	–

Table S5. Correlations between the measured and modeled concentrations of tracers for positive matrix factorization.

Tracers	Slope	R^2
WSOC	1.1	0.99
chloride	0.98	1.0
sulfate	0.97	0.94
sodium	0.98	1.0
MSA	1.0	1.0
sucrose	1.0	1.0
arabitol	0.98	0.99
trehalose	1.0	0.99
glucose	1.0	0.99
2-MGA	0.80	0.85
pinic acid	0.64	0.68
EC	0.95	1.0
levoglucosan	1.2	0.91
mannosan	0.94	0.73
hopane $C_{29}\alpha\beta$	0.93	0.95
BeP	0.96	0.94

Table S6. Diagnostics of the error estimation from BS (bootstrapping error estimate method) and DISP (displacement error estimate method).

BS Mapping (R ≥ 0.6)		Marine secondary aerosol	Biomass burning	FF-1	BSOA	Bioaerosol	Primary microorganism / plankton	FF-2	Marine primary emission	Unmapped
Marine secondary aerosol		89	0	5	4	0	0	0	1	0
Biomass burning		0	92	7	0	0	0	0	0	0
FF-1		0	0	89	2	1	1	5	1	0
BSOA		8	3	12	71	1	2	0	2	0
Bioaerosol		3	2	16	0	78	0	0	0	0
Primary microorganism / plankton		0	0	0	1	0	98	0	0	0
FF-2		2	0	0	0	1	0	93	0	3
Marine primary emission		0	0	0	0	0	0	0	99	0
DISP Diagnostics		Error Code: 0 Largest Decrease in Q: -0.228 (-0.05%)								
Factor Swaps	dQmax=4	0	0	0	0	0	0	0	0	
	dQmax=8	0	0	0	0	0	0	0	0	
	dQmax=15	0	0	0	0	0	0	0	0	
	dQmax=25	0	0	0	0	0	0	0	0	

Table S7. Contributions of different sources to the mass concentration of WSOC, the regressed MAEs for these sources, and the contributions of these sources to $b_{abs\text{-}365}$. These results are obtained by performing positive matrix factorization and non-negative multivariate linear regression.

Sources	Contribution to WSOC (%)	MAE (m^2 g^{-1})	Contribution to $b_{abs\text{-}365}$ (%)
BSOA	42 ± 23	0.22 ± 0.04	28 ± 24
Marine secondary aerosol	23 ± 18	–*	–
Marine primary emission	14 ± 13	0.04 ± 0.19	2.0 ± 2.8
Fossil fuel combustion	13 ± 14	2.3 ± 0.20	41 ± 34
Biomass burning	6.8 ± 4.3	1.4 ± 0.37	27 ± 21
Bioaerosol	2.6 ± 8.2	0.29 ± 0.48	1.6 ± 4.3

*: the regression coefficient (i.e., MAE) for marine secondary formation was firstly fitted to be < 0.0001 m^2 g^{-1} on average. Due to its negligible contribution to the light absorption, it is omitted from the final regression results.

Table S8. The simulated RAE of water-soluble BrC in our sample locations during the observation period.

Sources	Contribution (%)
Fossil fuel combustion	49 ± 7
Biomass burning	39 ± 8
BSOA	11 ± 2
Marine primary emission	0.9 ± 0.1

Table S9. Definitions of the eight molecular structural classes of molecules according to the criteria in Bianco et al. [15] and Xie et al. [16].

Classes	H/C	O/C
Lipid-like	(1.5, 2.0]	[0, 0.3]
Aliphatic / peptide-like	(1.5, 2.2]	(0.3, 0.67]
Carboxylic-rich alicyclic molecules-like / lignin-like	(0.67, 1.5]	[0.1, 0.67)
Carbohydrate-like	(1.5, 2.5]	(0.67, 1.2)
Unsaturated hydrocarbons	(0.67, 1.5]	< 0.1
Aromatic structures	[0.2, 0.67]	< 0.67
Highly oxygenated organic compounds / tannin-like	(0.6, 1.5]	[0.67, 1.2]
Others	Unclassified into the classes above	

Table S10. Contribution from different regions to bOC (OC from biomass burning) in the Arctic (North of 60°N).

Region	Contribution (%)
Mid-high latitude of Asia (north of 35°N, including Siberia)	~60
Mid-high latitude of North America (north of 35°N)	~30
Europe and other regions	~10

Table S11. The source-specific MAE_{365} of total BrC and the estimated contribution of each source to the light absorption of total BrC in the Arctic. For the light absorption of total BrC in the Arctic, biomass burning is still the dominant source (~60%).

Source	MAE_{365} ($m^2\ g^{-1}$)	Contribution to the light absorption of total BrC in the Arctic (%)
Biomass burning	0.61 ± 0.65	61
Fossil fuel combustion	0.18 ± 0.02	6.2
BSOA	0.14 ± 0.09	15
Marine primary emission	0.41 ± 0.15	18
Marine secondary aerosol	0.25 ± 0.51	–
Bioaerosol	1.6 ± 0.74	–
Primary microorganism / plankton	1.9 ± 3.5	–

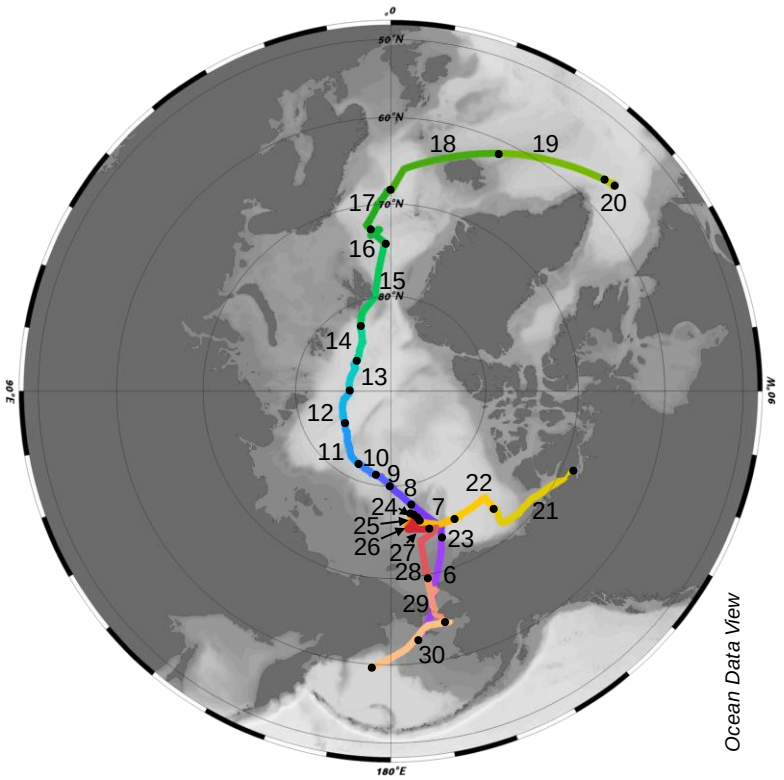

Fig. S1. Map of the cruise of Research Vessel *Xuelong* and sampling region for each filter from late July to September in 2017.

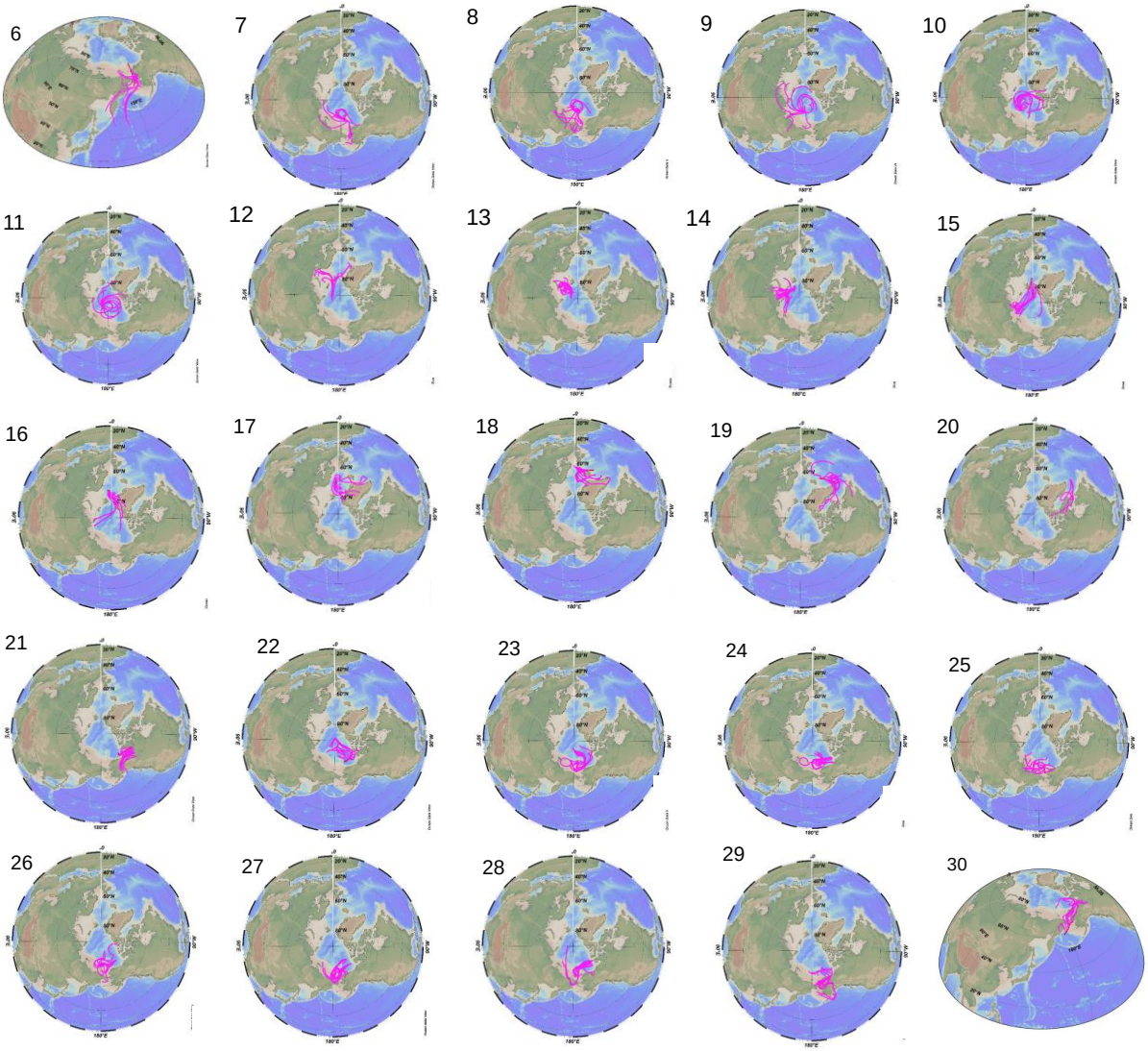

Fig. S2. 120-hour air mass back trajectories at 500 m calculated every 6 hours along the cruise. These plots are produced by the Hybrid Single-Particle Lagrangian Integrated Trajectory (HYSPLIT 4) model [17].

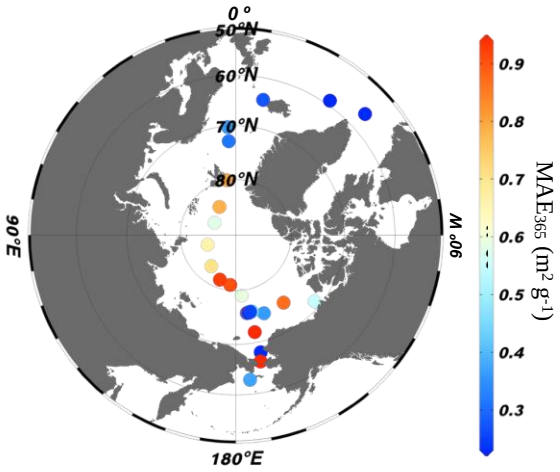

Fig. S3. Mass absorption efficiency at 365 nm (MAE_{365}, m^2 g^{-1}) along the circum-Arctic cruise. The plot is produced by Ocean Data View [18]. The color range is defined as the 10th and 90th percentiles of the measured MAE_{365}.

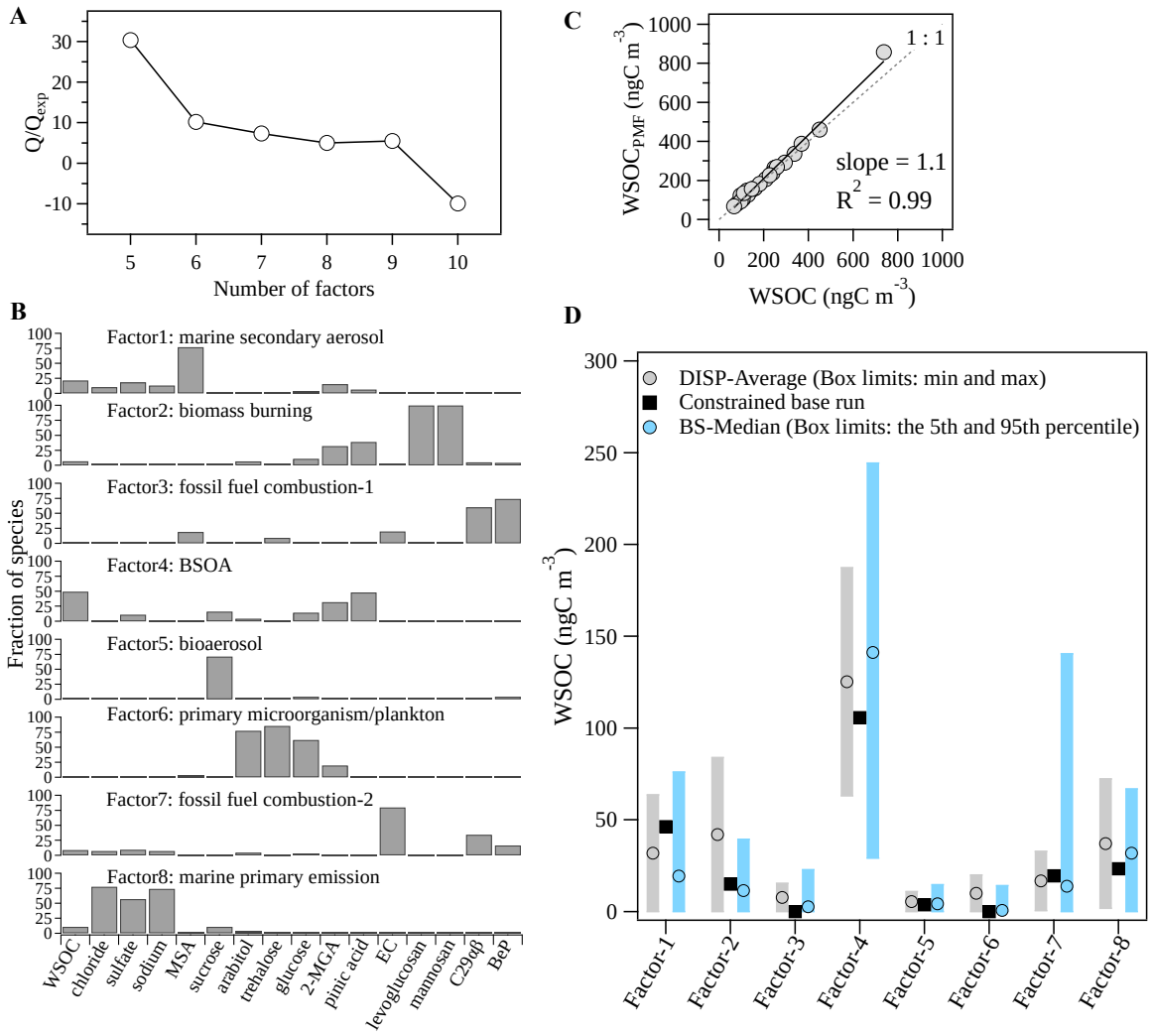

Fig. S4. The results and evaluation of the positive matrix factorization of the sources of WSOC. (**A**) The variation of Q/Q_{exp} with the increase of the number of factors in the positive matrix factorization analysis. (**B**) Factor profiles (percentage of each species in factor) for the 8-factor solution. (**C**) Scatter plot between the modelled and measured WSOC. (**D**) The error estimates for the modeled WSOC contribution from each factor. DISP (displacement error estimate method, see Experimental Procedures) and BS method (bootstrapping error estimate method) are shown along with the constrained base run.

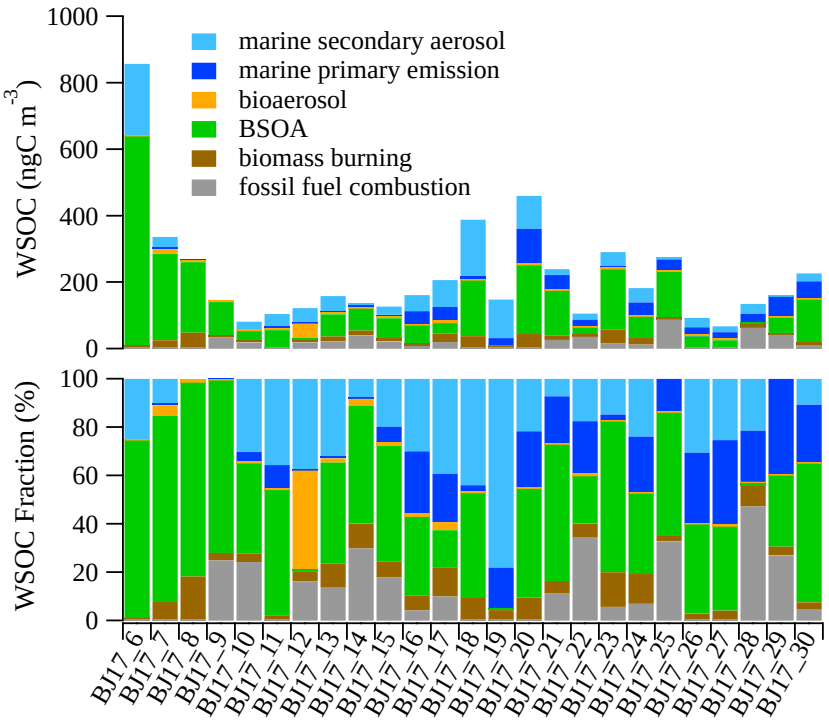

Fig. S5. The concentrations and relative fractions of different sources of WSOC for each sample in the circum-Arctic. The source apportionment is resolved by positive matrix factorization.

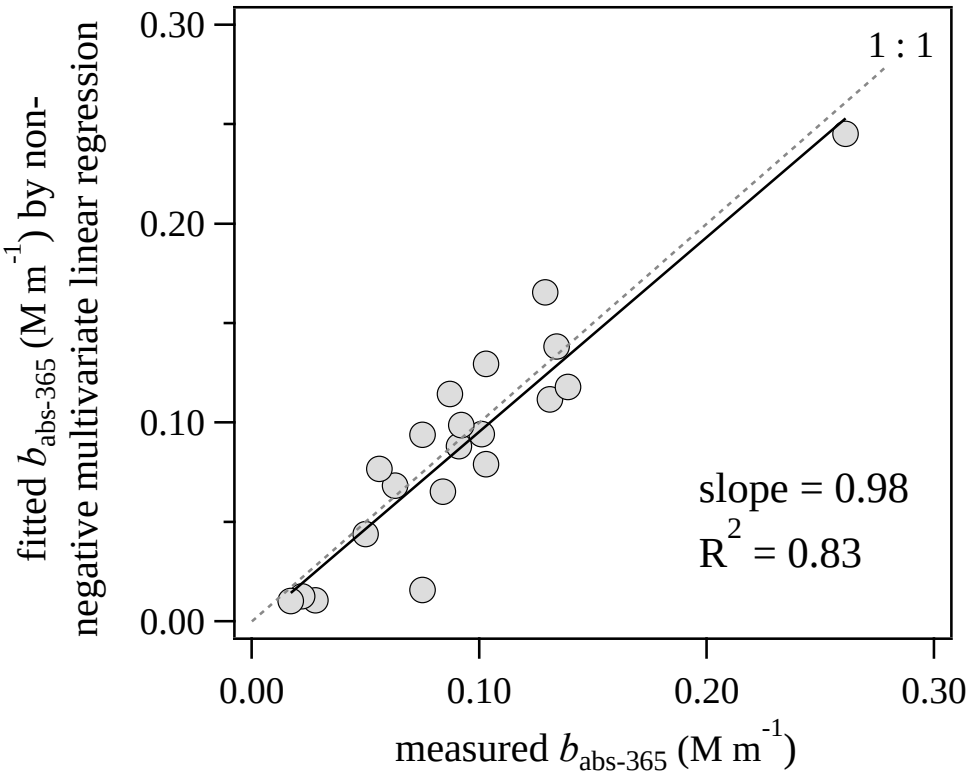

Fig. S6. The fitting of $b_{abs\text{-}365}$ by non-negative multivariate linear regression.

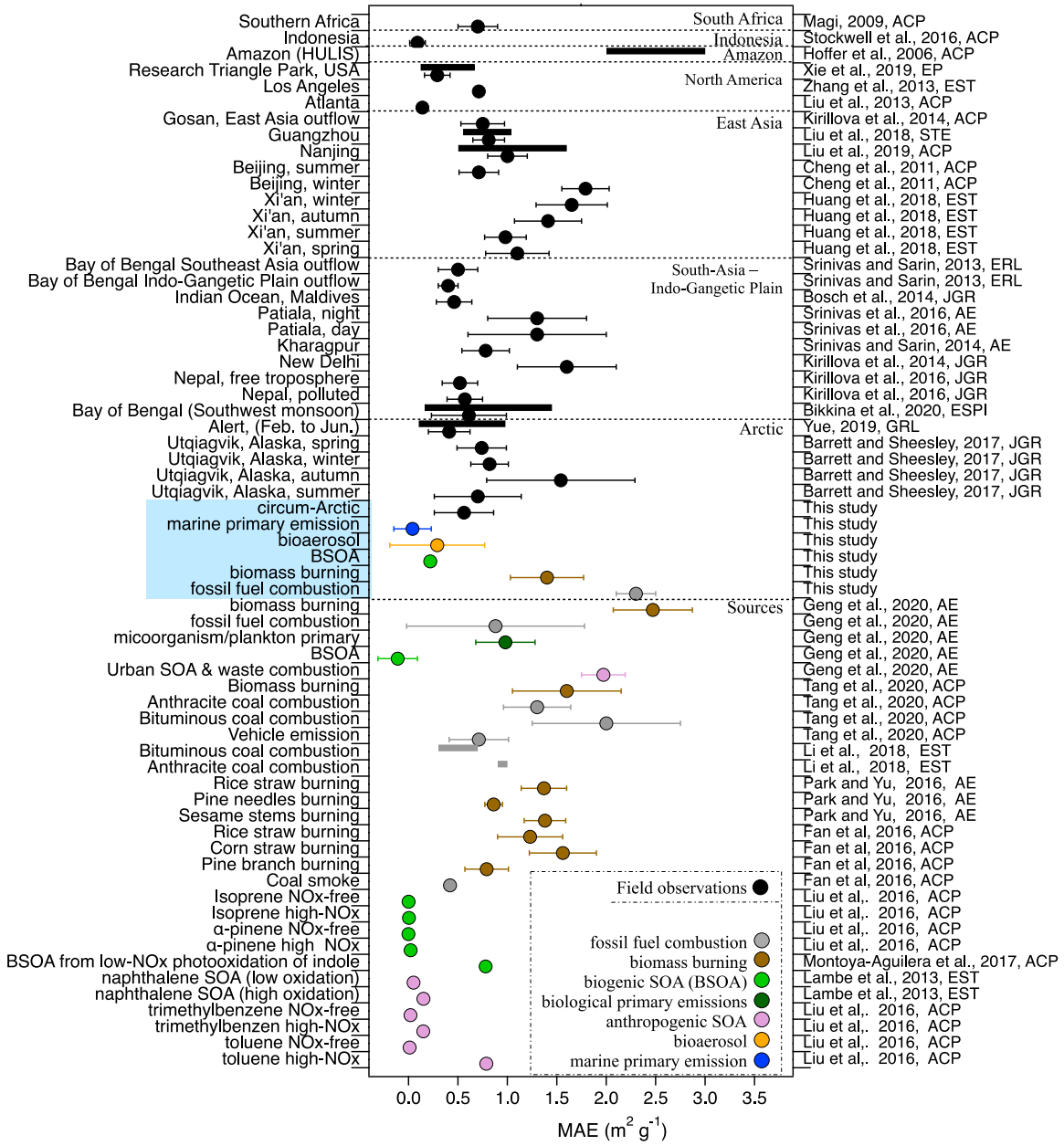

Fig. S7. MAE at 365 nm in this study, in source samples, and in previous reports in the Arctic, and other global hotpots of BrC, including South Asia–Indo Gangetic Plain, East Asia, North America, Amazon, Indonesia and southern Africa. Field observations are plotted in black. Measurements for source samples are plotted in other colors. MAEs are shown for average ± standard deviation (circles) and/or min-max range (bars). The values are extracted from these references: Magi [19] and Magi [20], Stockwell et al. [21], Hoffer et al. [22], Xie et al. [23], Zhang et al. [24], Liu et al. [25], Kirillova et al. [26], Liu et al. [27], Liu et al. [28], Cheng et al. [29], Huang et al. [30], Srinivas and Sarin [31], Bosch et al. [32], Srinivas et al. [33], Srinivas and Sarin [34], Kirillova et al. [35], Kirillova et al. [36], Bikkina et al. [37], Yue et al. [38], Barrett and Sheesley [39], Geng et al. [40], Tang et al. [41], Li et al. [42], Park and Yu [43], Fan et al. [44], Liu et al. [45], Montoya-Aguilera et al. [46], and Lambe et al. [47].

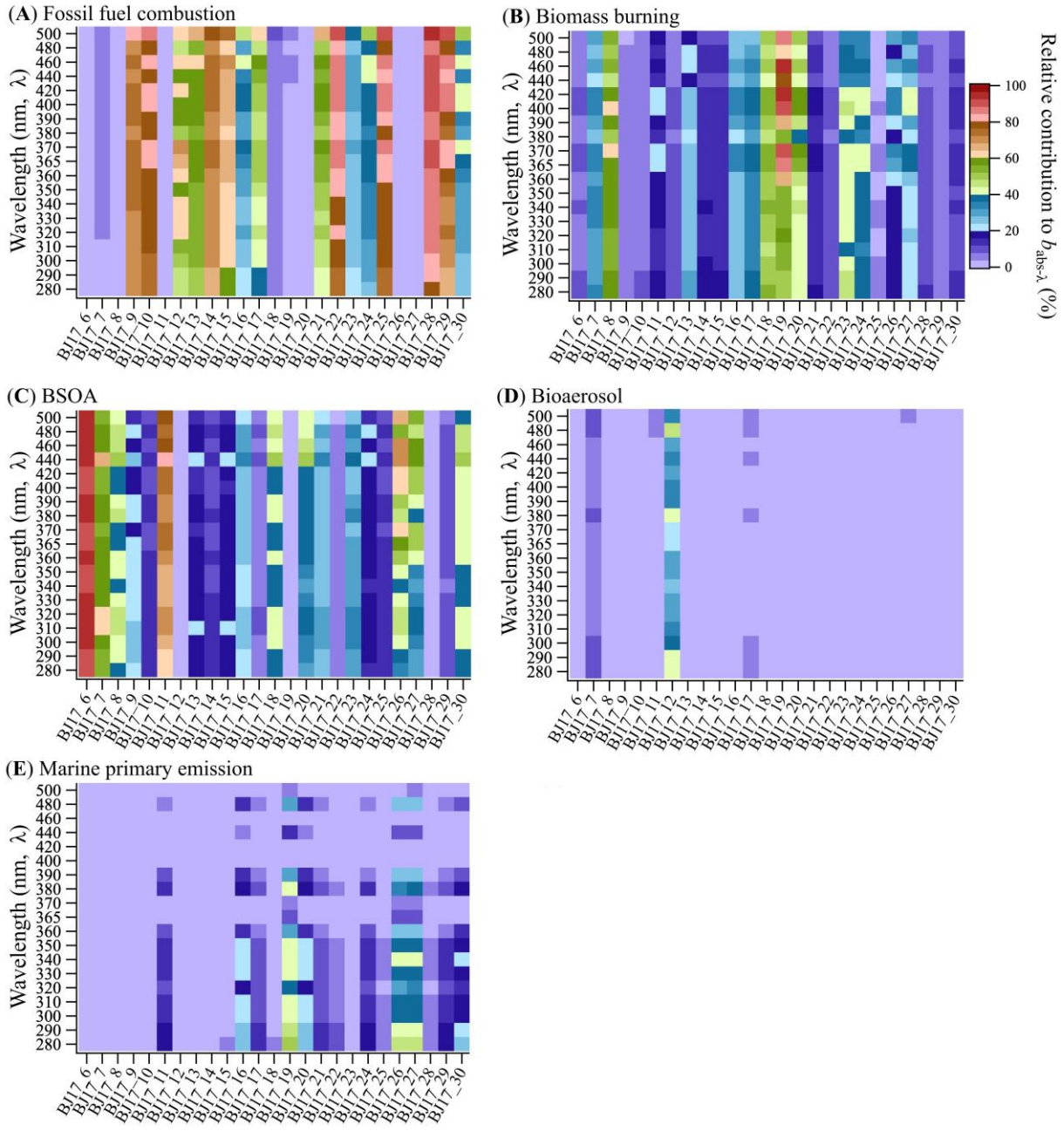

Fig. S8. Contributions of each source to the light absorption of water-soluble BrC (b_{abs}) at wavelengths from 280 nm to 500 nm in the circum-Arctic. (**A**) Fossil fuel combustion. (**B**) Biomass burning. (**C**) BSOA (biogenic SOA). (**D**) Bioaerosol. (**E**) Marine primary emission.

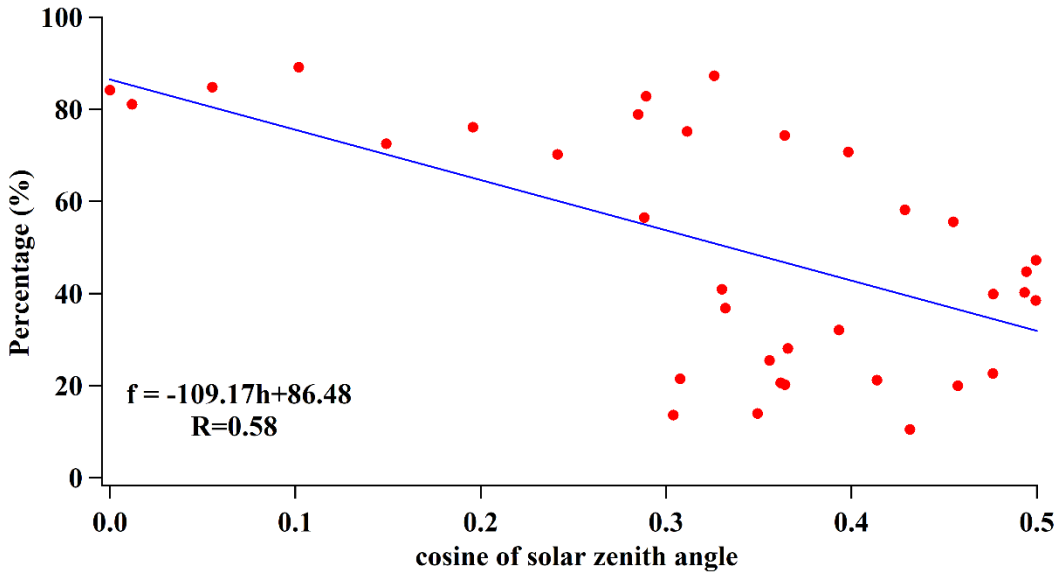

Fig. S9. The percentage of WSOC in the OC concentration versus the cosine of solar zenith angle. Water-soluble BrC is optically measured from WSOC. The blue line is the linear fitting. The observed percentages of WSOC in the OC concentration are from the circum-Arctic observation in this study and the observation at the Alert station in the Canadian high Arctic [38].

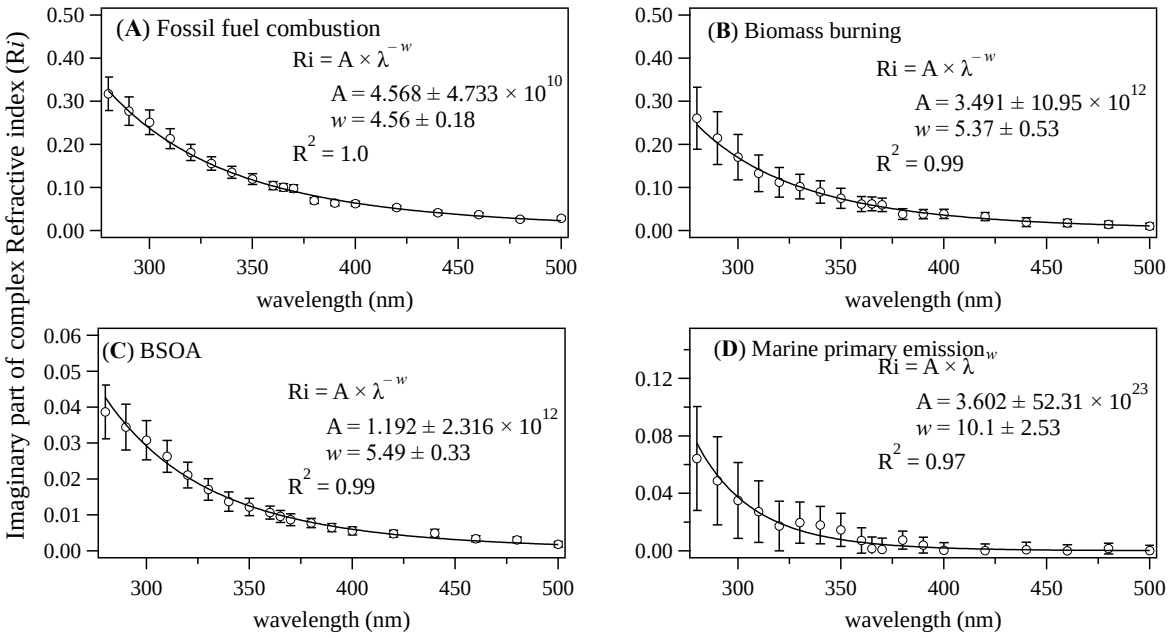

Fig. S10. The variation of the imaginary parts of complex refraction index (R*i*) with wavelength and the fitting of R*i* as a function of wavelength. These fitted functions were used as constraints in the modeling of the radiative effect of water-soluble BrC from these sources. The data are represented as mean ± standard deviation. Water-soluble BrC from four sources are included, which are (**A**) fossil fuel combustion, (**B**) biomass burning, (**C**) BSOA, and (**D**) marine primary emission. The parameter for water-soluble BrC from bioaerosol is not included because our model cannot simulate bioaerosol till now. However, this uncertainty is negligible because the contribution of bioaerosol is small as discussed in the main text.

A

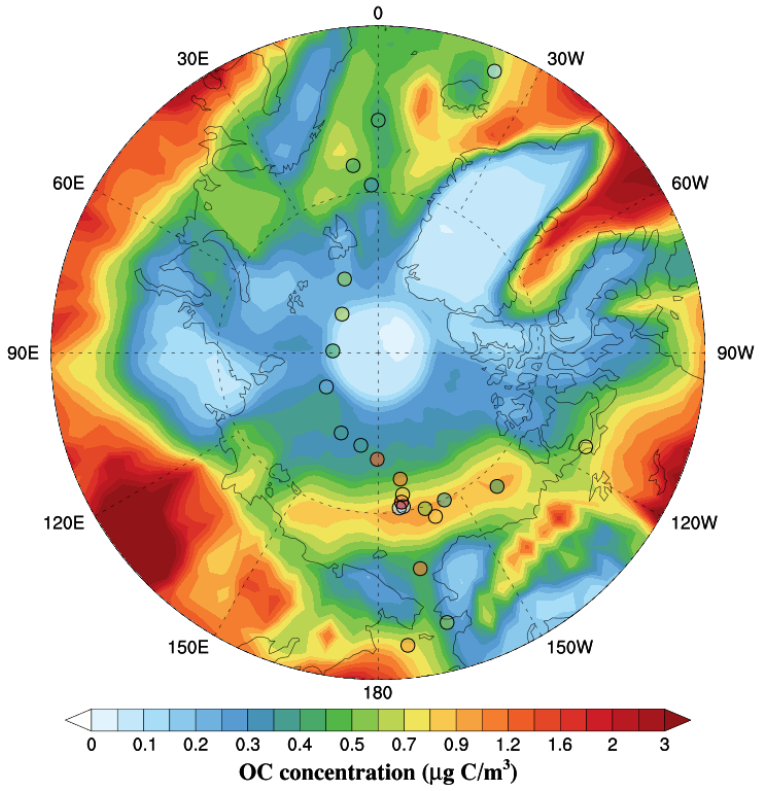

B

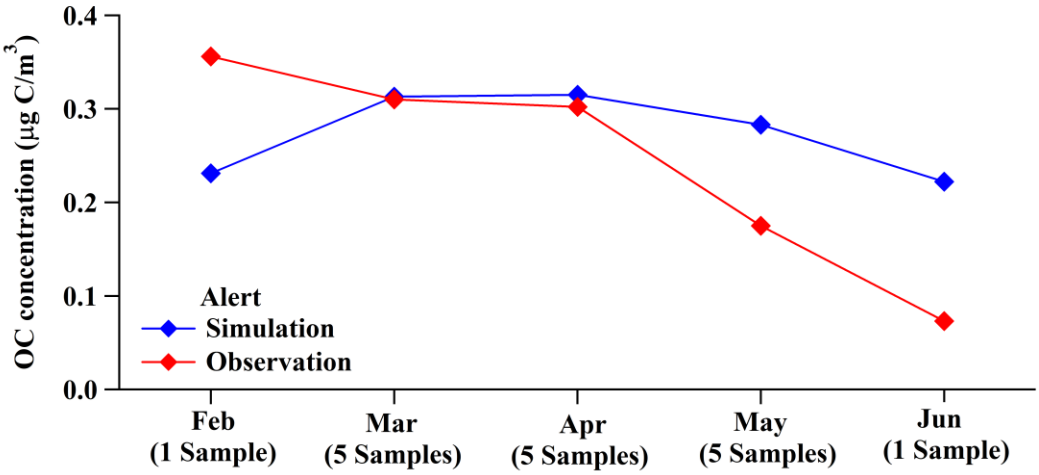

Fig. S11. Modelling ability evaluated by comparing with observations. (**A**) The simulated average OC concentration in the Arctic in August and September 2017. The circle markers are observed OC concentration of samples in the circum-Arctic. (**B**) Comparison of monthly average OC concentration in the Alert station between observation and simulation during February to June 1993. The observation data (red line) are from Yue *et al.* [38].

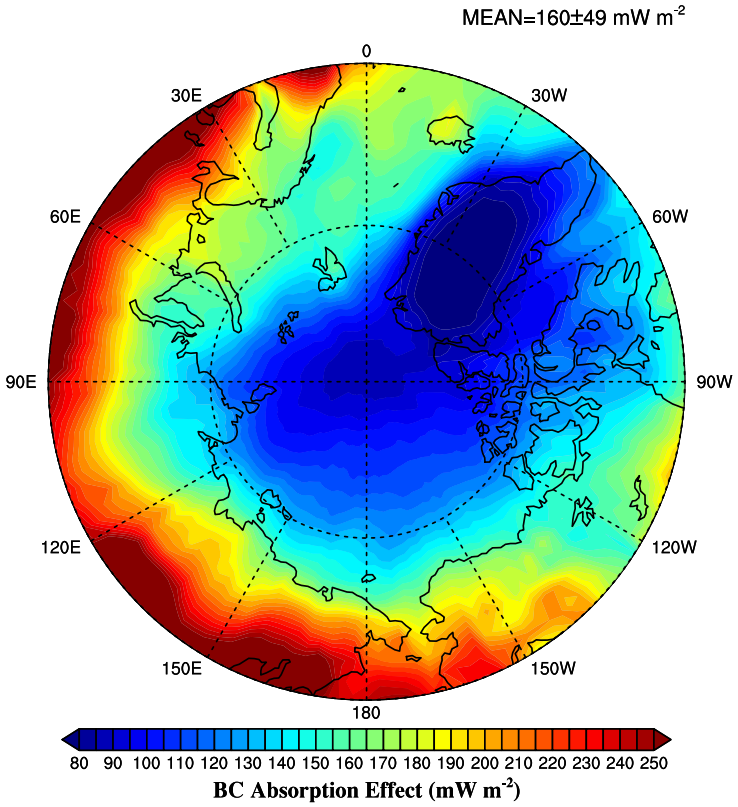

Fig. S12. The radiative absorption effect of BC in the Arctic.

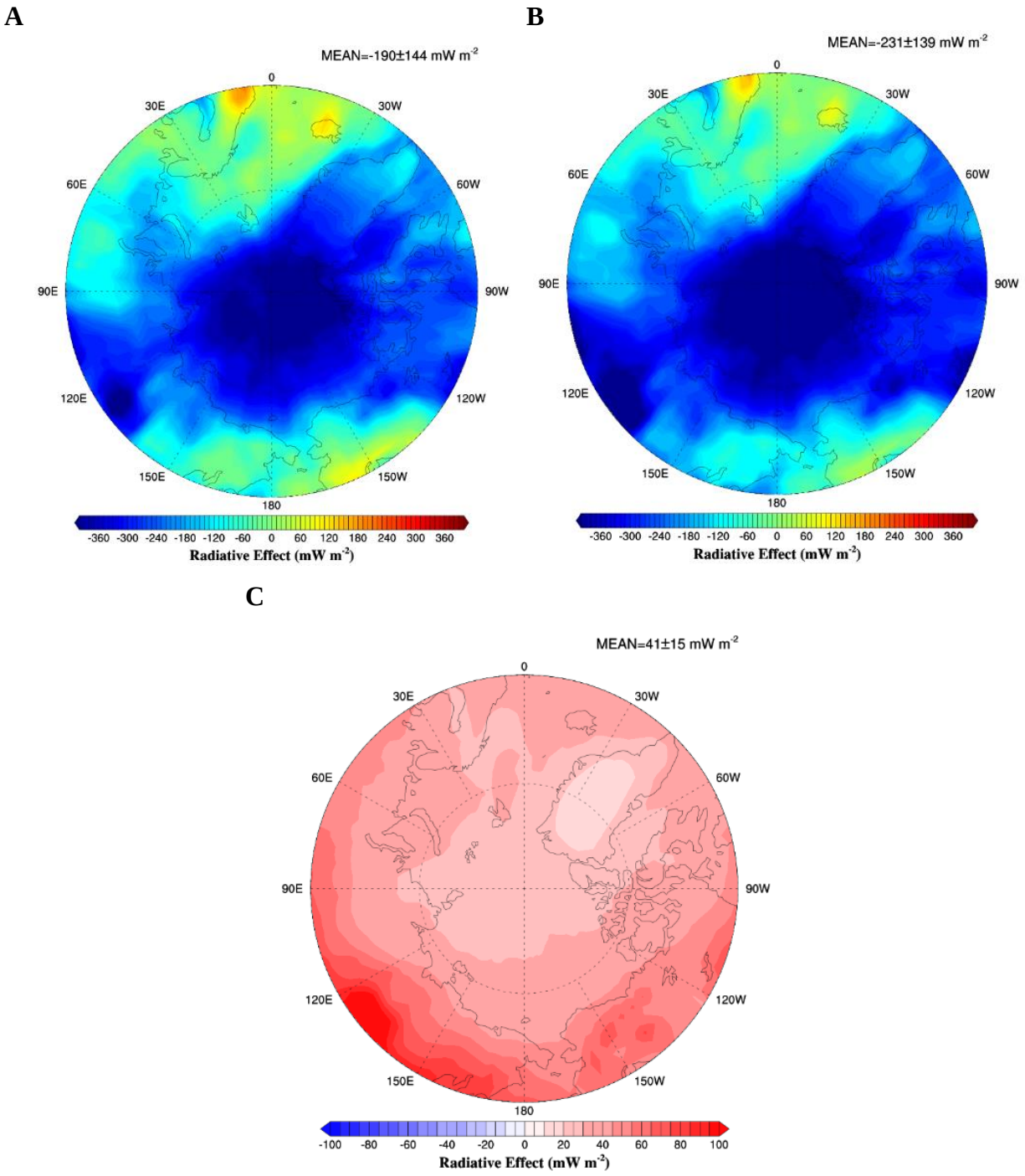

Fig. S13. The direct radiative effect of OC in the Arctic. The direct radiative effect of OC in the Arctic with (**A**) and without (**B**) absorption effect of water-soluble BrC as well as their difference (**C**).

A

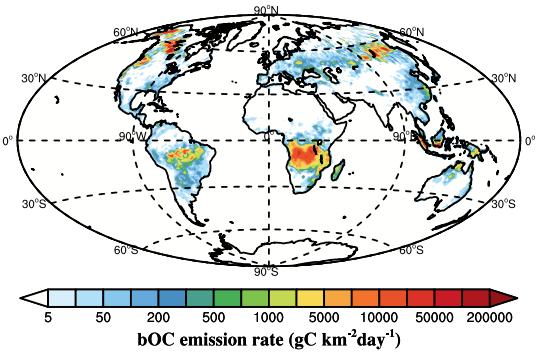

B

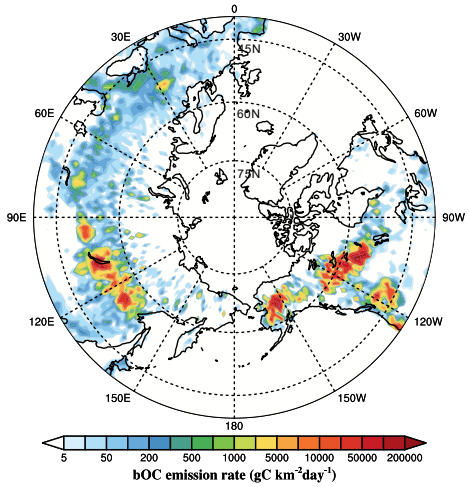

C

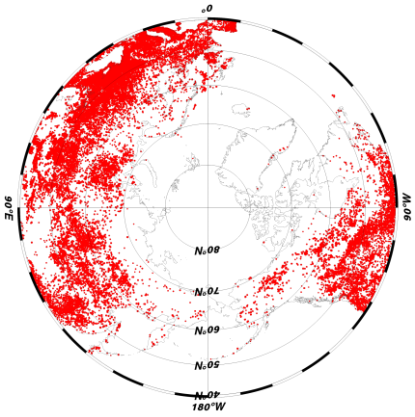

Fig. S14. The emission rate of OC from biomass burning (bOC) during summer (June-August). The emission rate of OC from biomass burning (bOC) during summer (June-August) over the world (**A**) and north of 40°N (**B**). (**C**) Fire spots north of 40ºN from June 1 to August 31 2017. The data is from NASA FIRMS VIIRS Fire/Hotspot (https://firms.modaps.eosdis.nasa.gov/).

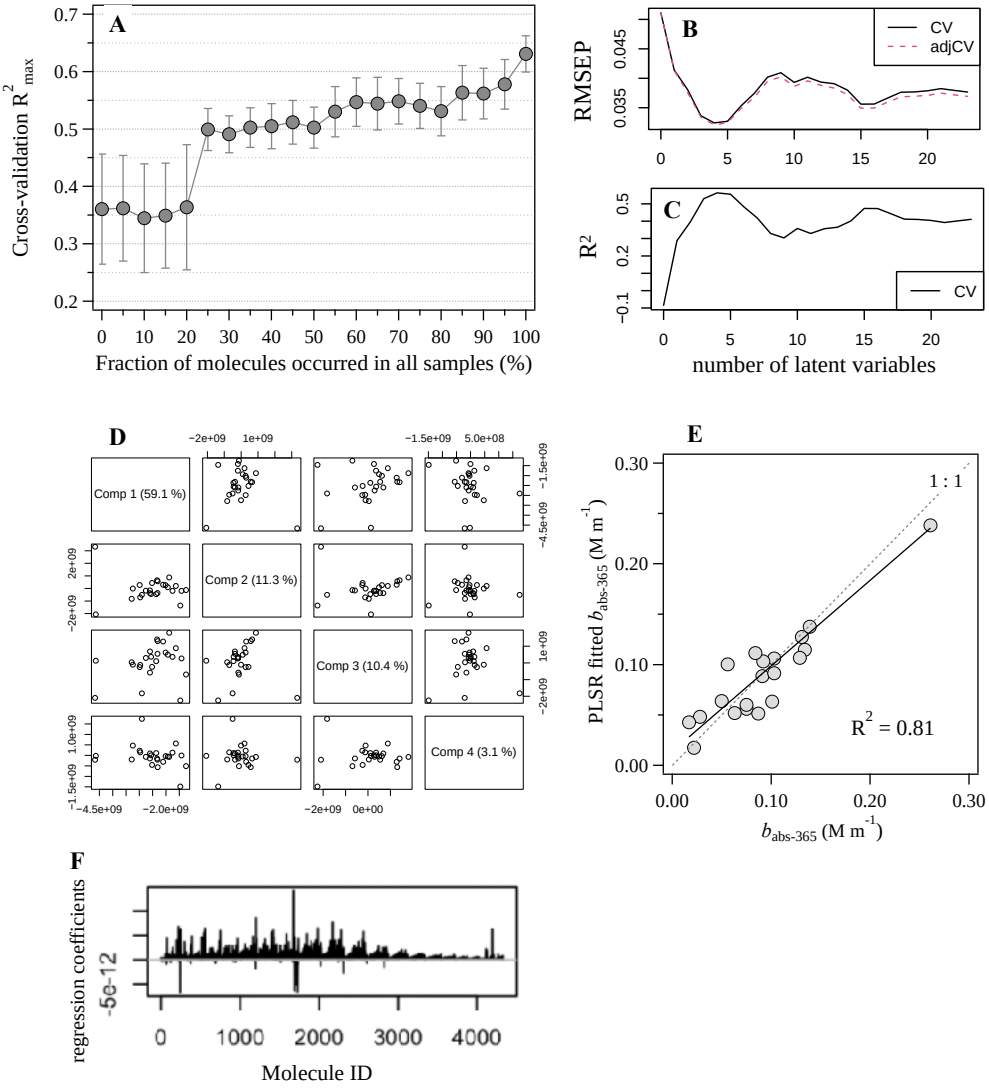

Fig. S15. Diagnostics of the partial least squares regression of $b_{abs\text{-}365}$ on the intensity of molecules measured by FT-ICR MS. (**A**) The variation of the cross-validation R^2 with the changing "$f_{molecule}$ dataset" of molecules, the definition of which is described in the Experimental Procedures in the main text. $f_{molecule}$, in percent, ranges from 0% to 100%. "0% dataset" represents a complete set of all molecules measured in any sample, while the "100% dataset" only includes molecules occurred in all samples, i.e., common molecules. (**B**) Variations of root mean squared error of prediction (RMSEP) and (**C**) R^2 with the increase of the number of components (i.e., latent variables) in the cross-validation for the final regression on the "60% dataset". CV is the ordinary cross-validation estimate, and adjCV is a bias-corrected cross-validation estimate. (**D**) Score plot of the regression on the "60% dataset". The low variance explained by the 4th component (3.1%) suggests three components is suitable for the regression fitting, which can avoid an over-fitting. (**E**) Scatter plot of the fitted and measured $b_{abs\text{-}365}$ for the regression on the "60% dataset". (**F**) Regression coefficients (i.e., the equivalent molecular absorption coefficients) of each molecule for the regression on the "60% dataset".

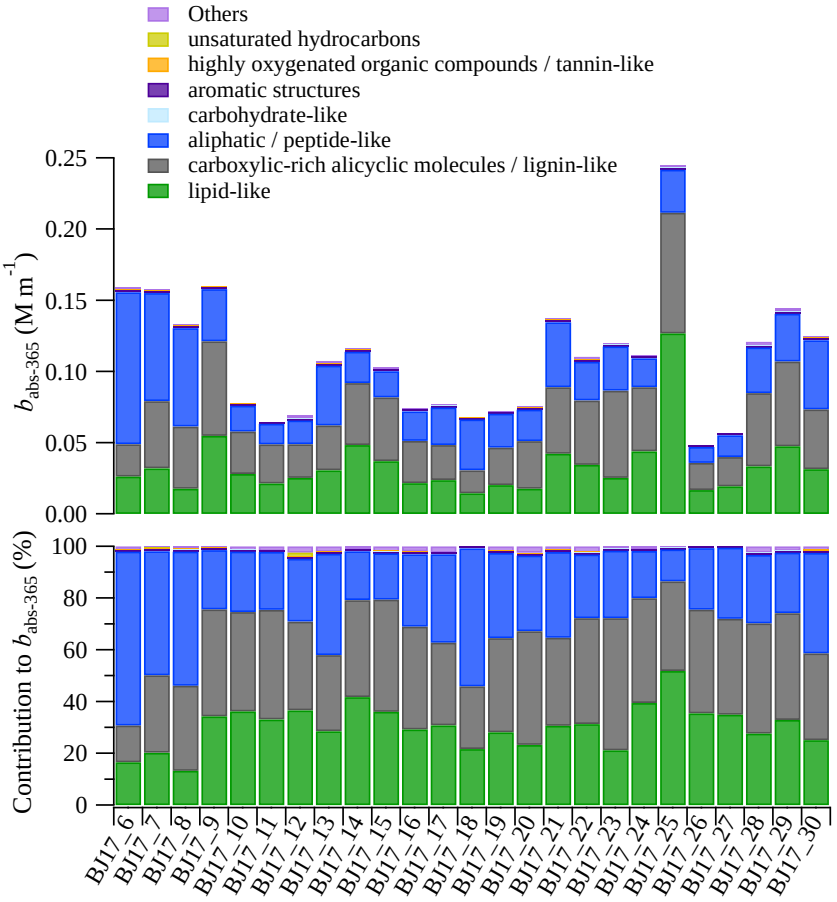

Fig. S16. Contributions of molecular structures to the total light absorption of water-soluble BrC at 365 nm ($b_{abs-365}$).

Supplemental References.

1. Timonen, H., Saarikoski, S., Tolonen-Kivimäki, O., Aurela, M., Saarnio, K., Petäjä, T., Aalto, P.P., Kulmala, M., Pakkanen, T., and Hillamo, R. (2008). Size distributions, sources and source areas of water-soluble organic carbon in urban background air. Atmos. Chem. Phys. *8*, 5635-5647. 10.5194/acp-8-5635-2008.
2. Suzuki, K., Kawamura, K., Kasukabe, H., Yanase, A., and Barrie, L.A. (1995). Concentration changes of MSA and major ions in Arctic aerosols during polar sunrise. Proc. NIPR Symp. Polar Meteorol. Glaciol *9*, 160-168. 10.15094/00003887.
3. Quinn, P.K., Collins, D.B., Grassian, V.H., Prather, K.A., and Bates, T.S. (2015). Chemistry and related properties of freshly emitted sea spray aerosol. Chem. Rev. *115*, 4383-4399. 10.1021/cr500713g.
4. Bates, T.S., Calhoun, J.A., and Quinn, P.K. (1992). Variations in the methanesulfonate to sulfate molar ratio in submicrometer marine aerosol particles over the south Pacific Ocean. J. Geophys. Res. Atmos. *97*, 9859-9865. 10.1029/92JD00411.
5. Graham, B., Guyon, P., Taylor, P.E., Artaxo, P., Maenhaut, W., Glovsky, M.M., Flagan, R.C., and Andreae, M.O. (2003). Organic compounds present in the natural Amazonian

aerosol: Characterization by gas chromatography–mass spectrometry. J. Geophys. Res. Atmos. *108*, 4766. 10.1029/2003JD003990.
6. Bauer, H., Claeys, M., Vermeylen, R., Schueller, E., Weinke, G., Berger, A., and Puxbaum, H. (2008). Arabitol and mannitol as tracers for the quantification of airborne fungal spores. Atmos. Environ. *42*, 588-593. 10.1016/j.atmosenv.2007.10.013.
7. Simoneit, B.R.T., Elias, V.O., Kobayashi, M., Kawamura, K., Rushdi, A.I., Medeiros, P.M., Rogge, W.F., and Didyk, B.M. (2004). SugarsDominant Water-Soluble Organic Compounds in Soils and Characterization as Tracers in Atmospheric Particulate Matter. Environ. Sci. Technol. *38*, 5939-5949. 10.1021/es0403099.
8. Ion, A.C., Vermeylen, R., Kourtchev, I., Cafmeyer, J., Chi, X., Gelencsér, A., Maenhaut, W., and Claeys, M. (2005). Polar organic compounds in rural PM2.5 aerosols from K-puszta, Hungary, during a 2003 summer field campaign: Sources and diel variations. Atmos. Chem. Phys. *5*, 1805-1814. 10.5194/acp-5-1805-2005.
9. Fu, P., Kawamura, K., Chen, J., and Barrie, L.A. (2009). Isoprene, monoterpene, and sesquiterpene oxidation products in the high Arctic aerosols during late winter to early summer. Environ. Sci. Technol. *43*, 4022-4028. 10.1021/es803669a.
10. Yu, J.Z., Cocker, D.R., Griffin, R.J., Flagan, R.C., and Seinfeld, J.H. (1999). Gas-phase ozone oxidation of monoterpenes: Gaseous and particulate products. J. Atmos. Chem. *34*, 207-258. 10.1023/A:1006254930583.
11. Zieman, J.J., Holmes, J.L., Connor, D., Jensen, C.R., Zoller, W.H., Hermann, D.M., Parrington, J.R., and Gordon, G.E. (1995). Atmospheric aerosol trace element chemistry at Mauna Loa observatory .1. 1979-1985. J. Geophys. Res. Atmos. *100*, 25979-25994. 10.1029/93jd03316.
12. Simoneit, B.R.T. (2002). Biomass burning - A review of organic tracers for smoke from incomplete combustion. Appl. Geochem. *17*, 129-162. 10.1016/S0883-2927(01)00061-0.
13. Schauer, J.J., Kleeman, M.J., Cass, G.R., and Simoneit, B.R.T. (1999). Measurement of emissions from air pollution sources. 2. C-1 through C-30 organic compounds from medium duty diesel trucks. Environ. Sci. Technol. *33*, 1578-1587. 10.1021/es980081n.
14. Rogge, W.F., Hildemann, L.M., Mazurek, M.A., Cass, G.R., and Simoneit, B.R.T. (1993). Sources of Fine Organic Aerosol .2. Noncatalyst and Catalyst-Equipped Automobiles and Heavy-Duty Diesel Trucks. Environ. Sci. Technol. *27*, 636-651. 10.1021/es00041a007.
15. Bianco, A., Deguillaume, L., Vaitilingom, M., Nicol, E., Baray, J.L., Chaumerliac, N., and Bridoux, M. (2018). Molecular Characterization of Cloud Water Samples Collected at the puy de Dôme (France) by Fourier Transform Ion Cyclotron Resonance Mass Spectrometry. Environ. Sci. Technol. *52*, 10275-10285. 10.1021/acs.est.8b01964.
16. Xie, Q., Su, S., Chen, S., Zhang, Q., Yue, S., Zhao, W., Du, H., Ren, H., Wei, L., Cao, D., et al. (2021). Molecular characterization of size-segregated organic aerosols in the urban boundary layer in wintertime Beijing by FT-ICR MS. Faraday Discuss. *226*, 457-478. 10.1039/D0FD00084A.
17. Stein, A.F., Draxler, R.R., Rolph, G.D., Stunder, B.J.B., Cohen, M.D., and Ngan, F. (2015). NOAA's HYSPLIT atmospheric transport and dispersion modeling system. Bull. Am. Meteorol. Soc. *96*, 2059-2077. 10.1175/BAMS-D-14-00110.1.
18. Schlitzer, R. (2021). Ocean Data View. https://odv.awi.de.
19. Magi, B.I. (2009). Chemical apportionment of southern African aerosol mass and optical depth. Atmos. Chem. Phys. *9*, 7643-7655. 10.5194/acp-9-7643-2009.

20. Magi, B.I. (2011). Corrigendum to "Chemical apportionment of southern African aerosol mass and optical depth" published in Atmos. Chem. Phys., 9, 7643–7655, 2009. Atmos. Chem. Phys. *11*, 4777-4778. 10.5194/acp-11-4777-2011.
21. Stockwell, C.E., Jayarathne, T., Cochrane, M.A., Ryan, K.C., Putra, E.I., Saharjo, B.H., Nurhayati, A.D., Albar, I., Blake, D.R., Simpson, I.J., et al. (2016). Field measurements of trace gases and aerosols emitted by peat fires in Central Kalimantan, Indonesia, during the 2015 El Nino. Atmos. Chem. Phys. *16*, 11711-11732. 10.5194/acp-16-11711-2016.
22. Hoffer, A., Gelencsér, A., Guyon, P., Kiss, G., Schmid, O., Frank, G.P., Artaxo, P., and Andreae, M.O. (2006). Optical properties of humic-like substances (HULIS) in biomass-burning aerosols. Atmos. Chem. Phys. *6*, 3563-3570. 10.5194/acp-6-3563-2006.
23. Xie, M.J., Chen, X., Holder, A.L., Hays, M.D., Lewandowski, M., Offenberg, J.H., Kleindienst, T.E., Jaoui, M., and Hannigan, M.P. (2019). Light absorption of organic carbon and its sources at a southeastern US location in summer. Environ. Pollut. *244*, 38-46. 10.1016/j.envpol.2018.09.125.
24. Zhang, X., Lin, Y.-H., Surratt, J.D., and Weber, R.J. (2013). Sources, Composition and Absorption Ångström Exponent of Light-absorbing Organic Components in Aerosol Extracts from the Los Angeles Basin. Environ. Sci. Technol. *47*, 3685-3693. 10.1021/es305047b.
25. Liu, J., Bergin, M., Guo, H., King, L., Kotra, N., Edgerton, E., and Weber, R.J. (2013). Size-resolved measurements of brown carbon in water and methanol extracts and estimates of their contribution to ambient fine-particle light absorption. Atmos. Chem. Phys. *13*, 12389-12404. 10.5194/acp-13-12389-2013.
26. Kirillova, E.N., Andersson, A., Han, J., Lee, M., and Gustafsson, Ö. (2014). Sources and light absorption of water-soluble organic carbon aerosols in the outflow from northern China. Atmos. Chem. Phys. *14*, 1413-1422. 10.5194/acp-14-1413-2014.
27. Liu, J., Mo, Y., Ding, P., Li, J., Shen, C., and Zhang, G. (2018). Dual carbon isotopes (14C and 13C) and optical properties of WSOC and HULIS-C during winter in Guangzhou, China. Sci. Total Environ. *633*, 1571-1578. 10.1016/j.scitotenv.2018.03.293.
28. Liu, X., Zhang, Y.-L., Peng, Y., Xu, L., Zhu, C., Cao, F., Zhai, X., Haque, M.M., Yang, C., and Chang, Y. (2019). Chemical and optical properties of carbonaceous aerosols in Nanjing, eastern China: regionally transported biomass burning contribution. Atmos. Chem. Phys. *19*, 11213-11233. 10.5194/acp-19-11213-2019.
29. Cheng, Y., He, K.B., Zheng, M., Duan, F.K., Du, Z.Y., Ma, Y.L., Tan, J.H., Yang, F.M., Liu, J.M., Zhang, X.L., et al. (2011). Mass absorption efficiency of elemental carbon and water-soluble organic carbon in Beijing, China. Atmos. Chem. Phys. *11*, 11497-11510. 10.5194/acp-11-11497-2011.
30. Huang, R.-J., Yang, L., Cao, J.-j., Chen, Y., Chen, Q., Li, Y., Duan, J., Zhu, C., Dai, W., Wang, K., et al. (2018). Brown Carbon Aerosol in Urban Xi'an, Northwest China: The Composition and Light Absorption Properties. Environ. Sci. Technol. *52*, 6825-6833. 10.1021/acs.est.8b02386.
31. Srinivas, B., and Sarin, M.M. (2013). Light absorbing organic aerosols (brown carbon) over the tropical Indian Ocean: impact of biomass burning emissions. Environ. Res. Lett. *8*, 44042. 10.1088/1748-9326/8/4/044042.
32. Bosch, C., Andersson, A., Kirillova, E.N., Budhavant, K., Tiwari, S., Praveen, P., Russell, L.M., Beres, N.D., Ramanathan, V., and Gustafsson, O. (2014). Source-diagnostic dual-isotope composition and optical properties of water-soluble organic

carbon and elemental carbon in the South Asian outflow intercepted over the Indian Ocean. J. Geophys. Res. Atmos. *119*, 11743-11759. 10.1002/2014JD022127.
33. Srinivas, B., Rastogi, N., Sarin, M.M., Singh, A., and Singh, D. (2016). Mass absorption efficiency of light absorbing organic aerosols from source region of paddy-residue burning emissions in the Indo-Gangetic Plain. Atmos. Environ. *125*, 360-370. 10.1016/j.atmosenv.2015.07.017.
34. Srinivas, B., and Sarin, M.M. (2014). Brown carbon in atmospheric outflow from the Indo-Gangetic Plain: Mass absorption efficiency and temporal variability. Atmos. Environ. *89*, 835-843. 10.1016/j.atmosenv.2014.03.030.
35. Kirillova, E.N., Andersson, A., Tiwari, S., Srivastava, A.K., Bisht, D.S., and Gustafsson, Ö. (2014). Water-soluble organic carbon aerosols during a full New Delhi winter: Isotope-based source apportionment and optical properties. J. Geophys. Res. Atmos. *119*, 3476-3485. 10.1002/2013jd020041.
36. Kirillova, E.N., Marinoni, A., Bonasoni, P., Vuillermoz, E., Facchini, M.C., Fuzzi, S., and Decesari, S. (2016). Light absorption properties of brown carbon in the high Himalayas. J. Geophys. Res. Atmos. *121*, 9621-9639. 10.1002/2016jd025030.
37. Bikkina, P., Bikkina, S., Kawamura, K., Sudheer, A.K., Mahesh, G., and Kumar, S.K. (2020). Evidence for brown carbon absorption over the Bay of Bengal during the southwest monsoon season: a possible oceanic source. Environmental Science: Processes & Impacts *22*, 1743-1758. 10.1039/d0em00111b.
38. Yue, S., Bikkina, S., Gao, M., Barrie, L.A., Kawamura, K., and Fu, P. (2019). Sources and Radiative Absorption of Water-Soluble Brown Carbon in the High Arctic Atmosphere. Geophys. Res. Lett. *46*, 14881-14891. 10.1029/2019GL085318.
39. Barrett, T.E., and Sheesley, R.J. (2017). Year-round optical properties and source characterization of Arctic organic carbon aerosols on the North Slope Alaska. J. Geophys. Res. Atmos. *122*, 9319-9331. 10.1002/2016jd026194.
40. Geng, X., Mo, Y., Li, J., Zhong, G., Tang, J., Jiang, H., Ding, X., Malik, R.N., and Zhang, G. (2020). Source apportionment of water-soluble brown carbon in aerosols over the northern South China Sea: Influence from land outflow, SOA formation and marine emission. Atmos. Environ. *229*, 117484. 10.1016/j.atmosenv.2020.117484.
41. Tang, J., Li, J., Su, T., Han, Y., Mo, Y., Jiang, H., Cui, M., Jiang, B., Chen, Y., Tang, J., et al. (2020). Molecular compositions and optical properties of dissolved brown carbon in biomass burning, coal combustion, and vehicle emission aerosols illuminated by excitation–emission matrix spectroscopy and Fourier transform ion cyclotron resonance mass spectrometry analysis. Atmos. Chem. Phys. *20*, 2513-2532. 10.5194/acp-20-2513-2020.
42. Li, M., Fan, X., Zhu, M., Zou, C., Song, J., Wei, S., Jia, W., and Peng, P.a. (2019). Abundance and Light Absorption Properties of Brown Carbon Emitted from Residential Coal Combustion in China. Environ. Sci. Technol. *53*, 595-603. 10.1021/acs.est.8b05630.
43. Park, S.S., and Yu, J. (2016). Chemical and light absorption properties of humic-like substances from biomass burning emissions under controlled combustion experiments. Atmos. Environ. *136*, 114-122. 10.1016/j.atmosenv.2016.04.022.
44. Fan, X., Wei, S., Zhu, M., Song, J., and Peng, P.a. (2016). Comprehensive characterization of humic-like substances in smoke PM2.5 emitted from the combustion of biomass materials and fossil fuels. Atmos. Chem. Phys. *16*, 13321-13340. 10.5194/acp-16-13321-2016.

45. Liu, J., Lin, P., Laskin, A., Laskin, J., Kathmann, S.M., Wise, M., Caylor, R., Imholt, F., Selimovic, V., and Shilling, J.E. (2016). Optical properties and aging of light-absorbing secondary organic aerosol. Atmos. Chem. Phys. *16*, 12815-12827. 10.5194/acp-16-12815-2016.
46. Montoya-Aguilera, J., Horne, J.R., Hinks, M.L., Fleming, L.T., Perraud, V., Lin, P., Laskin, A., Laskin, J., Dabdub, D., and Nizkorodov, S.A. (2017). Secondary organic aerosol from atmospheric photooxidation of indole. Atmos. Chem. Phys. *17*, 11605-11621. 10.5194/acp-17-11605-2017.
47. Lambe, A.T., Cappa, C.D., Massoli, P., Onasch, T.B., Forestieri, S.D., Martin, A.T., Cummings, M.J., Croasdale, D.R., Brune, W.H., Worsnop, D.R., and Davidovits, P. (2013). Relationship between Oxidation Level and Optical Properties of Secondary Organic Aerosol. Environ. Sci. Technol. *47*, 6349-6357. 10.1021/es401043j.